Advanced reproducing kernel meshfree modeling of cracked curved shells for mixed-mode stress resultant intensity factors

Ming-Jyun Dai[a], Satoyuki Tanaka[a,*], Shota Sadamoto[a,1], Tiantang Yu[b],
Tinh Quoc Bui[c]

[a]*Graduate School of Engineering, Hiroshima University, Japan,
e-mail: mingjyundai@gmail.com, satoyuki@hiroshima-u.ac.jp, shota.sadamoto@gmail.com*
[b]*Department of Engineering Mechanics, Hohai University, China,
e-mail: tiantangyu@hhu.edu.cn*
[c]*Department of Civil and Environmental Engineering,
Tokyo Institute of Technology, Japan, e-mail: bui.t.aa@m.titech.ac.jp*

Abstract

A meshfree approach for analyzing the fracture mechanics parameters in cracked curved shells is presented. The reproducing kernel (RK) meshfree method and mapping technique are employed to approximate cracked curvilinear surfaces and field variables. In order to model the crack segment, the meshfree discretization techniques are used. The stabilized conforming nodal integration (SCNI) and sub-domain stabilized conforming integration (SSCI) techniques are adopted to accurately integrate the stiffness matrix. The contour integral is chosen to evaluate the fracture mechanics parameters and discretized using the RKs and SSCI. The J-integral value is separated into symmetric and asymmetric components using the decomposition method to extract the mode-I and -II stress resultant intensity factors (SRIFs). The numerical results reveal that the accurate J-integral value and mixed-mode SRIFs of cracked curved shells can be effectively evaluated using the proposed formulation and discretization. The simplified fatigue crack propagation is also presented.

Keywords: Curved Shell; Fracture; Meshfree Method; Convected

---

[*]Corresponding author.
[1]Present address: Fujitsu Limited, 9-3, Nakase 1-chome, Mihama-ku, Chiba city, Chiba 261-8588, Japan

1. Introduction

Curved and cylindrical shells are typically used in engineering applications in the architectural, civil, offshore, and aerospace industries, owing to their high strength-to-weight ratio and high resistance for external loads. During the manufacturing process and in-service period, defects are occasionally included in structures. Under severe loads, it is possible that microcracks can be extended to form major cracks and lead to structural failure. The aim of fracture mechanics is to ensure the structural safety and integrity of cracked structural components. Fatigue and fracture analyses have been presented [1-5], and design rules have been published [6,7].

Fracture mechanics parameters, such as the J-integral value and stress intensity factors (SIFs) are mainly investigated with regard to two-dimensional and three-dimensional cracked solids [8,9]. Analytical solutions are restricted to problems with simple geometries and boundary conditions (BCs) [10,11]. Thus, numerical methods have been used for problems with complex geometries and BCs. The finite element method (FEM) is a popular numerical method. Although studies have analyzed cracked shell problems using the FEM [12-15], fracture mechanics simulations are still limited owing to difficulties in the crack modeling and re-meshing procedure. Recently alternative numerical methods, such as the dual boundary element method (BEM) [16], meshfree method [17-21], extended FEM (XFEM) [22], isogeometric analysis (IGA) [23,24], wavelet Galerkin method [25-29], and peridynamics [30-35] have been proposed to analyze various fracture problems. These methods have been extensively adopted to solve fracture problems for curved shells and cylinders. Dirgantara and Aliabadi solved cracked curved shells problems using the dual BEM [36]. Chau-Dinh *et al.* developed the Phantom-node method to evaluate the fracture mechanics parameters [37]. Nguyen-Thanh *et al.* [38] treated Kirchhoff-Love curved shells problems using the extended IGA. Xing *et al.* used the XFEM and Irwin's integral to deal with the fracture analysis for thin-walled structures including cracked cylinders [39]. Most studies have treated the J-integral value as a fracture mechanics parameter of cracked cylinders. To the authors' knowledge, only a few studies have analyzed the mixed-mode SIFs of cracked curved shells.

The authors have developed the Galerkin meshfree method for analyzing several shell structure problems. The RK [18] was adopted as the mesh-

free interpolant to approximate the membrane and bending deformations. A complete quadratic basis was imposed on the basis vector to satisfy the Kirchhoff mode reproducing condition [40,41]. Due to the lack of Kronecker delta property in the RKs, the singular kernel (SK) [42] was implemented to impose the essential BCs. The geometry was discretized using nodes, and the stiffness matrix was numerically integrated using SCNI [43,44] and SSCI [45-47]. Thus far, buckling problems had been considered for flat shells [48], stiffened plates [49,50], and curved shells [51,52]. Additionally, the fracture mechanics parameters had been analyzed for single-mode plate bending problems [53], mixed-mode membrane problems [54], mixed-mode plate bending problems [55], and fracture problems for stiffened plate and box beam structures [56]. Recently, geometrically nonlinear problems had been analyzed using the finite rotation meshfree formulation [57].

In the present study, the fracture analysis of cracked curved shells is conducted using the proposed Galerkin meshfree formulation and discretization. Because the RK is a smooth function, continuous stresses and strains can be obtained, which is suitable for evaluating the fracture mechanics parameters. By employing the RKs and the mapping technique based on the convected coordinate system (CCS) [51,52,58], arbitrary curvilinear shell geometries and field variables are tractable. To model fracture phenomena in a curved shell, the diffraction method, visibility criterion [59], and enriched basis [60] are used. Additionally, SCNI and SSCI are employed as numerical integration techniques for the stiffness matrix. The contour integral is chosen to analyze the fracture mechanics parameters. The J-integral value is separated into symmetric and asymmetric components to extract the mixed-mode SRIFs using the decomposition method [61,62]. Moreover, the model is extended to consider cracked cylinders and solve the single and mixed-mode SRIFs. All calculated results for the J-integral value and mixed-mode SRIFs are compared with reference solutions to examine the accuracy of the proposed approach.

The rest of this paper is structured as follows. The meshfree formulation and discretization for cracked curved shells and cracked cylinders are presented in Section 2. The evaluation of the fracture mechanics parameters is discussed in Section 3. Several numerical examples are shown in Section 4. The conclusions drawn from this study are given in Section 5.

2. Galerkin meshfree formulation and discretization for cracked curved shell

The meshfree formulation and discretization are presented for analyzing cracked curved shells. The mapping technique based on the CCS is applied to model an arbitrary curved shell from a flat plate. Both geometries and field variables are approximated using the RKs. The Mindlin-Reissner plate theory is adopted for the plate bending deformation, and the plane stress condition is employed for the in-plane deformation. A homogeneous, isotropic, and elastic material is assumed throughout shell structures.

2.1. Shell kinematics

Thus far, buckling problems for intact curved shells [51] and cracked curved shells [50] have been analyzed in previous studies using the shell kinematics formulations. This paper briefly introduces the basic formulation concepts.

A schematic illustration of a curved shell including a through crack is shown in Fig. 1. The domain of a curved shell is Ω, and its boundary is Γ. The traction force $\bar{t}$ is applied to the force boundary Γ_t, and the displacement $\bar{u}$ is prescribed on the displacement boundary Γ_u. Γ_c is the crack segment. Γ_{Jint} is a contour for evaluating the fracture mechanics parameters. $\boldsymbol{X}=(X_1, X_2, X_3)$ is the position vector on the global Cartesian coordinate system. The orthogonal unit vector is $\boldsymbol{e}_i$ (i=1,2,3). $\boldsymbol{r}=(r^1, r^2, r^3)$ is the position vector on the CCS. The shell thickness is t_h, and r^1-r^2 is the mid-thickness plane of a curved shell. $\boldsymbol{V}_i$ is the orthogonal unit vector of the local coordinate system. These are related as: $\boldsymbol{V}_2 = \frac{\boldsymbol{V}_3 \times \boldsymbol{e}_1}{|\boldsymbol{V}_3 \times \boldsymbol{e}_1|}$ and $\boldsymbol{V}_1 = \boldsymbol{V}_2 \times \boldsymbol{V}_3$.

In the shell kinematics, the position vector $\boldsymbol{X}$ and displacement vector $\boldsymbol{u}$ of a curved shell can be written as:

$$\boldsymbol{X} = \boldsymbol{X}_{\mathrm{mid}} + \frac{r^3}{2} t_h \boldsymbol{V}_3, \tag{1}$$

$$\boldsymbol{u} = \boldsymbol{u}_{\mathrm{mid}} + \frac{r^3}{2} t_h (-\theta_1 \boldsymbol{V}_2 + \theta_2 \boldsymbol{V}_1), \tag{2}$$

where $\boldsymbol{X}_{\mathrm{mid}}$ and $\boldsymbol{u}_{\mathrm{mid}}$ are the position vector and displacement vector on the mid-thickness plane, respectively. θ_1 and θ_2 are the rotation components in

terms of $\boldsymbol{V}_1$ and $\boldsymbol{V}_2$, respectively. The displacement vector $\boldsymbol{u}=\{u_1\ u_2\ u_3\}^T$ of an arbitrary point is written as:

$$\boldsymbol{u} = \left\{ \begin{array}{l} u_{\text{mid}1} - \frac{t_{\text{h}}}{2}r^3\theta_1 V_{2(1)} + \frac{t_{\text{h}}}{2}r^3\theta_2 V_{1(1)} \\ u_{\text{mid}2} - \frac{t_{\text{h}}}{2}r^3\theta_1 V_{2(2)} + \frac{t_{\text{h}}}{2}r^3\theta_2 V_{1(2)} \\ u_{\text{mid}3} - \frac{t_{\text{h}}}{2}r^3\theta_1 V_{2(3)} + \frac{t_{\text{h}}}{2}r^3\theta_2 V_{1(3)} \end{array} \right\}, \tag{3}$$

where $u_{\text{mid}i}$ denotes the components of $\boldsymbol{u}_{\text{mid}}$, and $V_{i(j)}$ is the dot product of $\boldsymbol{V}_i$ and $\boldsymbol{e}_j$.
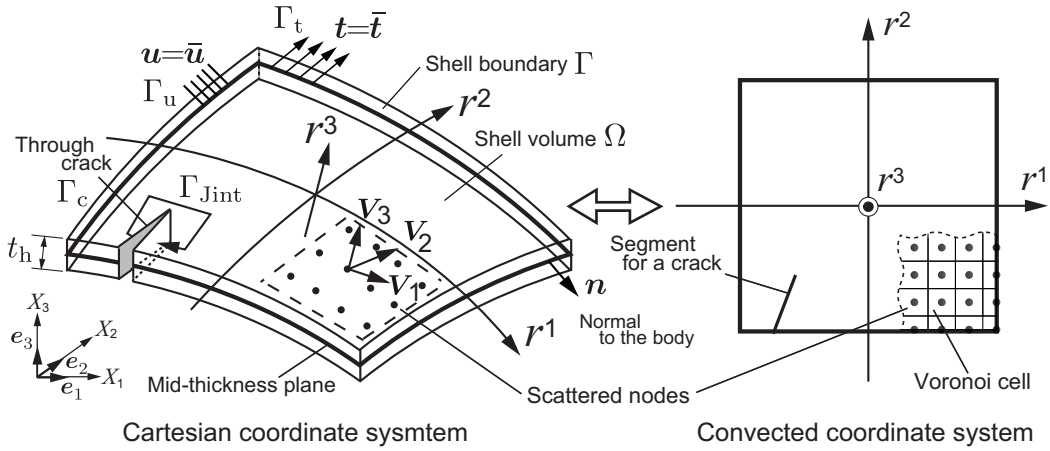
Figure 1: Schematic illustration of curved shell and mapping technique based on the CCS.

2.2. Representation of position and displacement vectors

In the meshfree discretization, the nodes are distributed on the mid-thickness plane, and the RKs are constructed for each node on the CCS as shown in Fig. 1. The Voronoi cell is employed in the numerical integration of the stiffness matrix. The position vector $\boldsymbol{X}(\boldsymbol{r})$ and displacement vector $\boldsymbol{u}(\boldsymbol{r})$ are interpolated by the RKs, respectively, as:

$$\boldsymbol{X}(\boldsymbol{r}) = \sum_{I=1}^{\text{NP}} \psi_I(r^1, r^2) \left(\boldsymbol{X}_{\text{mid}I} + \frac{r^3}{2}t_{\text{h}}\boldsymbol{V}_{3I} \right), \tag{4}$$

$$\boldsymbol{u}(\boldsymbol{r}) = \sum_{I=1}^{\text{NP}} \psi_I(r^1, r^2) \left(\boldsymbol{u}_{\text{mid}I} + \frac{r^3}{2}t_{\text{h}}\boldsymbol{V}_{3I} \right), \tag{5}$$

where $\psi_I(r^1, r^2)$ is the RK of the I-th node. $\boldsymbol{X}_{\mathrm{mid}I}$ and $\boldsymbol{u}_{\mathrm{mid}I}$ are the position and displacement vectors on the mid-thickness plane, respectively. $\boldsymbol{V}_{3I}$ is the unit director. NP is the total number of the scattered nodes. The concept is similar to the isoparametric FEM, therefore, the completeness condition can be satisfied.

The RK $\psi_I(=\psi_I(r^1, r^2))$ is written as:

$$\psi_I = \boldsymbol{h}^T(r_I^1 - r^1, r_I^2 - r^2)\boldsymbol{b}(r^1, r^2)\phi_I(r_I^1 - r^1, r_I^2 - r^2), \tag{6}$$

where $\boldsymbol{h}(r_I^1 - r^1, r_I^2 - r^2)(=\{1 \ \ r^1 \ \ r^2 \ \ (r^1)^2 \ \ r^1 r^2 \ \ (r^2)^2\})$ is the basis vector. The complete quadratic basis is chosen. $\boldsymbol{b}(r^1, r^2)$ is the coefficient vector. $\phi_I(r_I^1 - r^1, r_I^2 - r^2)$ is the original kernel function. The cubic spline function is taken as:

$$\phi_I(r_I^1 - r^1, r_I^2 - r^2) = \frac{10}{7\pi h_I^2} \begin{cases} 1 - \frac{3}{2}s_I^2 + \frac{3}{4}s_I^3 & (0 \le s_I \le 1) \\ \frac{1}{4}(2 - s_I)^3 & (1 \le s_I \le 2) \\ 0 & (2 \le s_I) \end{cases}, \tag{7}$$

where $s_I(=\sqrt{(r_I^1 - r^1)^2 + (r_I^2 - r^2)^2}/h_I)$ is the normalized distance from the center of the kernel. h_I is a parameter for defining the function support. The function support of the RKs is set from 2.5 to 2.7 of the characteristic length between the I-th node and its neighboring particles.

The visibility criterion, diffraction method [59], and enriched basis [60] are adopted to model the fracture in a curved shell. The details of the fracture modeling have been reported in [53-56]. The visibility criterion is employed to represent the displacement discontinuity. When the function support intersects the crack segment, double nodes are set along the crack segment, and the function support on the opposite side is cut as represented in Fig. 2(a). Here, x_1' and x_2' denote the local coordinate system at the crack tip. The diffraction method is introduced when the function support includes the crack tip. Hence, the function support is modified to wrap around the crack tip as shown in Fig. 2(a). The original function support s_I for the I-th node in Eq. (7) is modified as:

$$\hat{s}_I = \left(\frac{s_1 + s_2(\boldsymbol{r})}{s_0(\boldsymbol{r})}\right)^\lambda \frac{s_0(\boldsymbol{r})}{h_I}, \tag{8}$$

where $s_0(\boldsymbol{r})=||\boldsymbol{r} - \boldsymbol{r}_I||$, $s_1=||\boldsymbol{r}_c - \boldsymbol{r}_I||$, and $s_2(\boldsymbol{r})=||\boldsymbol{r} - \boldsymbol{r}_c||$ are the normalized distances, as shown in Fig. 2(a). Here, λ is set to 1.0. The enriched basis is

6

adopted to effectively represent the stress singularity around the crack tip. An additional term is included in the basis vector expressed in Eq. (6), *i.e.*, $\boldsymbol{h}(r_I^1 - r^1, r_I^2 - r^2) = \{1 \quad r^1 \quad r^2 \quad (r^1)^2 \quad r^1 r^2 \quad (r^2)^2 \quad \sqrt{\rho'}\sin(\theta'/2)\}$; ρ' and θ' denote the local polar coordinate system at the crack tip.

In this study, SCNI and SSCI are employed to numerically integrate the stiffness matrix. A schematic illustration of the meshfree discretization is shown in Fig. 2(b). SCNI is used throughout the curved shell, while SSCI is employed along the crack segment and around the crack tip. The discretization of the stiffness matrix is presented in the following section.
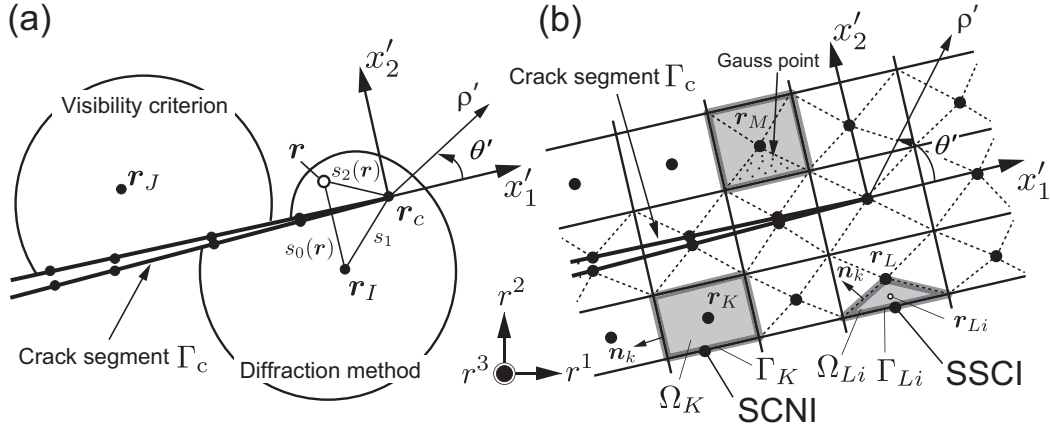
Figure 2: Crack modeling and its meshfree discretization. [(a) crack modeling employing the diffraction method and visibility criterion, (b) meshfree discretization with SCNI and SSCI].

The displacement vector can be discretized using the RKs, as:

$$\boldsymbol{u}(\boldsymbol{r}) = \sum_{I=1}^{\text{NP}} \boldsymbol{\Psi}_I \boldsymbol{U}_I, \tag{9}$$

$$\boldsymbol{\Psi}_I = \sum_{I=1}^{\text{NP}} \begin{bmatrix} \psi_I & 0 & 0 & -\frac{t_h}{2}r^3\psi_I V_{2(1)} & \frac{t_h}{2}r^3\psi_I V_{1(1)} \\ 0 & \psi_I & 0 & -\frac{t_h}{2}r^3\psi_I V_{2(2)} & \frac{t_h}{2}r^3\psi_I V_{1(2)} \\ 0 & 0 & \psi_I & -\frac{t_h}{2}r^3\psi_I V_{2(3)} & \frac{t_h}{2}r^3\psi_I V_{1(3)} \end{bmatrix}, \tag{10}$$

where $\boldsymbol{U}_I = \{u_{\text{mid}1I} \quad u_{\text{mid}2I} \quad u_{\text{mid}3I} \quad \theta_{1I} \quad \theta_{2I}\}^T$ is the displacement coefficient vector of the I-th node.

Covariant and contravariant base vectors are introduced to transform the physical values between the global Cartesian coordinate system and the CCS. The covariant base vectors can be evaluated using the partial derivative of the position vector $\boldsymbol{X}$ with respect to the r^i-axis, $i.e.$, $\boldsymbol{G}_i = \partial \boldsymbol{X}/\partial r^i$. According to Eq. (4), the partial derivatives can be presented as:

$$\frac{\partial \boldsymbol{X}}{\partial r^i} = \sum_{I=1}^{\mathrm{NP}} \frac{\partial \psi_I(r^1, r^2)}{\partial r^i} \left(\boldsymbol{X}_{\mathrm{mid}I} + \frac{r^3}{2} t_{\mathrm{h}} \boldsymbol{V}_{3I} \right), \quad (i = 1, 2),$$

$$\frac{\partial \boldsymbol{X}}{\partial r^3} = \sum_{I=1}^{\mathrm{NP}} \psi_I(r^1, r^2) \frac{1}{2} t_{\mathrm{h}} \boldsymbol{V}_{3I}. \tag{11}$$

The contravariant base vectors $\boldsymbol{G}^i$ can be derived from the covariant base vectors, as: $\boldsymbol{G}^i = \frac{\boldsymbol{G}_j \times \boldsymbol{G}_k}{\boldsymbol{G}_i \cdot (\boldsymbol{G}_j \times \boldsymbol{G}_k)}$ where $(i, j, k) = (1,2,3), (2,3,1), (3,1,2)$.

2.3. Galerkin meshfree formulation and discretization

A cracked curved shell shown in Fig. 1 is considered. The governing equation of elastostatic problems can be written as:

$$\nabla \cdot \boldsymbol{\sigma} = 0 \quad \text{in} \quad \Omega, \tag{12}$$

$$\boldsymbol{\sigma}^T \cdot \boldsymbol{n} = 0 \quad \text{on} \quad \Gamma_{\mathrm{c}}, \tag{13}$$

$$\boldsymbol{\sigma}^T \cdot \boldsymbol{n} = \bar{\boldsymbol{t}} \quad \text{on} \quad \Gamma_{\mathrm{t}}, \tag{14}$$

$$\boldsymbol{u} = \bar{\boldsymbol{u}} \quad \text{on} \quad \Gamma_{\mathrm{u}}, \tag{15}$$

where $\boldsymbol{\sigma}$ is the Cauchy stress, and $\boldsymbol{n}$ is the normal vector to the body. For a cracked curved shell without the body force term, the principle of virtual work can be written as:

$$\int_{\Omega} \boldsymbol{\varepsilon}(\delta \boldsymbol{u}) : \boldsymbol{C} : \boldsymbol{\varepsilon}(\boldsymbol{u}) d\Omega - \delta W = 0,$$

$$\delta W = \int_{\Gamma_{\mathrm{t}}} \delta \boldsymbol{u} \cdot \bar{\boldsymbol{t}} \, d\Gamma, \tag{16}$$

where $\boldsymbol{\varepsilon}$ is the strain tensor. $\boldsymbol{C}$ is the elastic constitutive tensor. W is the external virtual work. δ represents the variations. SKs are adopted to impose the displacement BCs on Γ_{u}.

The displacement-strain relationship is derived using the covariant and contravariant base vectors, and it can be written as:

$$\boldsymbol{\varepsilon} = \frac{1}{2}\left(\boldsymbol{G}_i \cdot \frac{\partial \boldsymbol{u}}{\partial r^j} + \boldsymbol{G}_j \cdot \frac{\partial \boldsymbol{u}}{\partial r^i}\right)\boldsymbol{G}^i \otimes \boldsymbol{G}^j$$
$$= \varepsilon_{ij}\boldsymbol{G}^i \otimes \boldsymbol{G}^j. \tag{17}$$

The strain components ε_{ij} are written in vector form as [58]:

$$\varepsilon_{ij} = \left\{\begin{array}{c} \varepsilon_{11} \\ \varepsilon_{22} \\ 2\varepsilon_{12} \\ 2\varepsilon_{23} \\ 2\varepsilon_{31} \end{array}\right\} = \left[\begin{array}{c} \boldsymbol{G}_1 \cdot \frac{\partial \boldsymbol{u}}{\partial r^1} \\ \boldsymbol{G}_2 \cdot \frac{\partial \boldsymbol{u}}{\partial r^2} \\ \boldsymbol{G}_1 \cdot \frac{\partial \boldsymbol{u}}{\partial r^2} + \boldsymbol{G}_2 \cdot \frac{\partial \boldsymbol{u}}{\partial r^1} \\ \boldsymbol{G}_2 \cdot \frac{\partial \boldsymbol{u}}{\partial r^3} + \boldsymbol{G}_3 \cdot \frac{\partial \boldsymbol{u}}{\partial r^2} \\ \boldsymbol{G}_3 \cdot \frac{\partial \boldsymbol{u}}{\partial r^1} + \boldsymbol{G}_1 \cdot \frac{\partial \boldsymbol{u}}{\partial r^3} \end{array}\right], \tag{18}$$

where $\partial \boldsymbol{u}/\partial r^i$ (i=1,2,3) is the partial derivative of the displacement vector $\boldsymbol{u}$ with respect to the r^i-axis. It is given in matrix form, as:

$$\frac{\partial \boldsymbol{u}}{\partial r^i} = \sum_{I=1}^{\text{NP}} \left[\begin{array}{ccccc} \frac{\partial \psi_I}{\partial r^i} & 0 & 0 & -A_{i2(1)} & A_{i1(1)} \\ 0 & \frac{\partial \psi_I}{\partial r^i} & 0 & -A_{i2(2)} & A_{i1(2)} \\ 0 & 0 & \frac{\partial \psi_I}{\partial r^i} & -A_{i2(3)} & A_{i1(3)} \end{array}\right] \boldsymbol{U}_I$$
$$= \sum_{I=1}^{\text{NP}} \boldsymbol{\Psi}_{I,i}\boldsymbol{U}_I, \quad (i = 1, 2), \tag{19}$$

$$\frac{\partial \boldsymbol{u}}{\partial r^3} = \sum_{I=1}^{\text{NP}} \left[\begin{array}{ccccc} 0 & 0 & 0 & -\frac{t_{\text{h}}}{2}\psi_I V_{2(1)} & \frac{t_{\text{h}}}{2}\psi_I V_{1(1)} \\ 0 & 0 & 0 & -\frac{t_{\text{h}}}{2}\psi_I V_{2(2)} & \frac{t_{\text{h}}}{2}\psi_I V_{1(2)} \\ 0 & 0 & 0 & -\frac{t_{\text{h}}}{2}\psi_I V_{2(3)} & \frac{t_{\text{h}}}{2}\psi_I V_{1(3)} \end{array}\right] \boldsymbol{U}_I$$
$$= \sum_{I=1}^{\text{NP}} \boldsymbol{\Psi}_{I,3}\boldsymbol{U}_I, \tag{20}$$

where $\boldsymbol{\Psi}_{I,i}$ is the partial derivative of the RKs with respect to the r^i-axis. $A_{ij(k)}$ is the dot product of the vector $\boldsymbol{A}_{i1}$ or $\boldsymbol{A}_{i2}$ and unit vector $\boldsymbol{e}_k$. The component $\boldsymbol{A}_{ij}$ can be written as:

$$\boldsymbol{A}_{ij} = \frac{t_{\text{h}}}{2}r^3\left(\frac{\partial \psi_I}{\partial r^i}\boldsymbol{V}_j + \psi_I\frac{\partial \boldsymbol{V}_j}{\partial r^i}\right). \tag{21}$$

The displacement-strain matrix $\boldsymbol{B}_I$ for the I-th node is derived from the strain components ε_{ij}. By substituting the derivatives of the displacement

9

vector in Eqs. (19) and (20) into the strain tensor in Eq. (18), $\boldsymbol{B}_I$ can be obtained as:

$$\varepsilon_{ij} = \sum_{I=1}^{NP} \begin{bmatrix} \boldsymbol{G}_1^T \boldsymbol{\Psi}_{I,1} \\ \boldsymbol{G}_2^T \boldsymbol{\Psi}_{I,2} \\ \boldsymbol{G}_1^T \boldsymbol{\Psi}_{I,2} + \boldsymbol{G}_2^T \boldsymbol{\Psi}_{I,1} \\ \boldsymbol{G}_2^T \boldsymbol{\Psi}_{I,3} + \boldsymbol{G}_3^T \boldsymbol{\Psi}_{I,2} \\ \boldsymbol{G}_3^T \boldsymbol{\Psi}_{I,1} + \boldsymbol{G}_1^T \boldsymbol{\Psi}_{I,3} \end{bmatrix} \boldsymbol{U}_I$$

$$= \sum_{I=1}^{NP} \boldsymbol{B}_I \boldsymbol{U}_I. \tag{22}$$

The components of $\boldsymbol{B}_I$ are given in matrix form, as:

$$\boldsymbol{B}_I = \begin{bmatrix} \boldsymbol{G}_{1(1)}\frac{\partial\psi_I}{\partial r^1} & \boldsymbol{G}_{1(2)}\frac{\partial\psi_I}{\partial r^1} & \boldsymbol{G}_{1(3)}\frac{\partial\psi_I}{\partial r^1} \\ \boldsymbol{G}_{2(1)}\frac{\partial\psi_I}{\partial r^2} & \boldsymbol{G}_{2(2)}\frac{\partial\psi_I}{\partial r^2} & \boldsymbol{G}_{2(3)}\frac{\partial\psi_I}{\partial r^2} \\ \boldsymbol{G}_{2(1)}\frac{\partial\psi_I}{\partial r^1}+\boldsymbol{G}_{1(1)}\frac{\partial\psi_I}{\partial r^2} & \boldsymbol{G}_{2(2)}\frac{\partial\psi_I}{\partial r^1}+\boldsymbol{G}_{1(2)}\frac{\partial\psi_I}{\partial r^2} & \boldsymbol{G}_{2(3)}\frac{\partial\psi_I}{\partial r^1}+\boldsymbol{G}_{1(3)}\frac{\partial\psi_I}{\partial r^2} \\ \boldsymbol{G}_{3(1)}\frac{\partial\psi_I}{\partial r^2} & \boldsymbol{G}_{3(2)}\frac{\partial\psi_I}{\partial r^2} & \boldsymbol{G}_{3(3)}\frac{\partial\psi_I}{\partial r^2} \\ \boldsymbol{G}_{3(1)}\frac{\partial\psi_I}{\partial r^1} & \boldsymbol{G}_{3(2)}\frac{\partial\psi_I}{\partial r^1} & \boldsymbol{G}_{3(3)}\frac{\partial\psi_I}{\partial r^1} \end{bmatrix}$$

$$\begin{matrix} -\boldsymbol{G}_1 \cdot \boldsymbol{A}_{12} & \boldsymbol{G}_1 \cdot \boldsymbol{A}_{11} \\ -\boldsymbol{G}_2 \cdot \boldsymbol{A}_{22} & \boldsymbol{G}_2 \cdot \boldsymbol{A}_{21} \\ -\boldsymbol{G}_2 \cdot \boldsymbol{A}_{12} - \boldsymbol{G}_1 \cdot \boldsymbol{A}_{22} & \boldsymbol{G}_2 \cdot \boldsymbol{A}_{11} + \boldsymbol{G}_1 \cdot \boldsymbol{A}_{21} \\ -\boldsymbol{G}_3 \cdot \boldsymbol{A}_{22} - \frac{t_{\mathrm{h}}}{2}\psi_I\, \boldsymbol{G}_2 \cdot \boldsymbol{V}_2 & \boldsymbol{G}_3 \cdot \boldsymbol{A}_{21} + \frac{t_{\mathrm{h}}}{2}\psi_I\, \boldsymbol{G}_2 \cdot \boldsymbol{V}_1 \\ -\boldsymbol{G}_3 \cdot \boldsymbol{A}_{12} - \frac{t_{\mathrm{h}}}{2}\psi_I\, \boldsymbol{G}_1 \cdot \boldsymbol{V}_2 & \boldsymbol{G}_3 \cdot \boldsymbol{A}_{11} + \frac{t_{\mathrm{h}}}{2}\psi_I\, \boldsymbol{G}_1 \cdot \boldsymbol{V}_1 \end{matrix} \Bigg], \tag{23}$$

where $\boldsymbol{G}_{i(j)}$ is the dot product of $\boldsymbol{G}_i$ and $\boldsymbol{e}_j$.

The constitutive equation for an elastic material can be written as:

$$\boldsymbol{\sigma} = \boldsymbol{C} : \boldsymbol{\varepsilon}, \tag{24}$$

where $\boldsymbol{\sigma}\,(=\sigma^{ij}\boldsymbol{G}_i \otimes \boldsymbol{G}_j)$ is the Cauchy stress, and $\boldsymbol{C}$ is the fourth-order elastic tensor, which can be given by the orthogonal unit vectors, as:

$$\boldsymbol{C} = C_{ijkl}\boldsymbol{V}_i \otimes \boldsymbol{V}_j \otimes \boldsymbol{V}_k \otimes \boldsymbol{V}_l, \tag{25}$$

where the coefficient matrix C_{ijkl} is written as:

$$
C_{ijkl} =
\begin{bmatrix}
C_{1111} & C_{1122} & C_{1112} & C_{1123} & C_{1131} \\
C_{2211} & C_{2222} & C_{2212} & C_{2223} & C_{2231} \\
C_{1211} & C_{1222} & C_{1212} & C_{1223} & C_{1231} \\
C_{2311} & C_{2322} & C_{2312} & C_{2323} & C_{2331} \\
C_{3111} & C_{3122} & C_{3112} & C_{3123} & C_{3131}
\end{bmatrix}
$$

$$
= \frac{E}{1-\nu^2}
\begin{bmatrix}
1 & \nu & & & \\
& 1 & & 0 & \\
& & \frac{1-\nu}{2} & & \\
& \text{sym.} & & \kappa_{\mathrm{s}}\frac{1-\nu}{2} & \\
& & & & \kappa_{\mathrm{s}}\frac{1-\nu}{2}
\end{bmatrix},
\tag{26}
$$

where $\kappa_{\mathrm{s}}=\pi^2/12$ is the shear correction factor. E and ν are Young's modulus and Poisson's ratio, respectively. The tensor $\boldsymbol{C}$ can be written based on the covariant and contravariant base vectors, as:

$$
\boldsymbol{C} = C^{ijkl}\boldsymbol{G}_i \otimes \boldsymbol{G}_j \otimes \boldsymbol{G}_k \otimes \boldsymbol{G}_l.
\tag{27}
$$

The coefficient matrix has the following relationship:

$$
C^{ijkl} = C_{mnop}(\boldsymbol{V}_m \cdot \boldsymbol{G}^i)(\boldsymbol{V}_n \cdot \boldsymbol{G}^j)(\boldsymbol{V}_o \cdot \boldsymbol{G}^k)(\boldsymbol{V}_p \cdot \boldsymbol{G}^l).
\tag{28}
$$

2.4. Numerical integration techniques of stiffness matrix

As shown in Fig. 2(b), SCNI and SSCI [53-55] are introduced as numerical integration techniques. The analysis domain is divided by a number of Voronoi cells. The entire domain is numerically integrated by SCNI, while SSCI is employed for the domain around the crack tip. For simplicity, the displacement components are rewritten as: $\{u_1 \quad u_2 \quad u_3 \quad u_4 \quad u_5\}(= \{u_{\mathrm{mid1}} \quad u_{\mathrm{mid2}} \quad u_{\mathrm{mid3}} \quad \theta_1 \quad \theta_2\})$.

With Gauss' divergence theorem to the partial derivative of the displacement components $u_{j,k}(\boldsymbol{r})$, the domain integration form can be transformed into the contour integration form. The physical values are smoothed in the entire cell. SCNI for a cell in terms of the K-th node $\boldsymbol{r}_K$ in Fig. 2(b) can be

derived as:

$$\tilde{u}_{j,k}^{h}(\boldsymbol{r}_K) = \frac{1}{A_K} \int_{\Omega_K} u_{j,k}^{h}(\boldsymbol{r}) \, d\Omega$$

$$= \frac{1}{A_K} \int_{\Gamma_K} u_j^{h}(\boldsymbol{r}) n_k \, d\Gamma = \sum_{I=1}^{\mathrm{NP}} b_{Ik}(\boldsymbol{r}_K) u_{jI},$$

$$b_{Ik}(\boldsymbol{r}_K) = \frac{1}{A_K} \int_{\Gamma_K} \psi_I(\boldsymbol{r}) n_k \, d\Gamma, \quad j = \{1, \cdots, 5\}, \quad k = \{1, 2\}, \qquad (29)$$

where (˜) denotes the smoothed values. Ω_K and Γ_K are the domain and boundary of a Voronoi cell in terms of the K-th node, respectively, as shown in Fig. 2(b). A_K is the area of Ω_K. n_k is the normal vector to the boundary Γ_K. Moreover, SSCI is employed for the domain around the crack tip. As shown in Fig. 2(b), the Voronoi cell is further divided into a number of triangular sub-domains Ω_{L_i}. SSCI is carried out for sub-domains, and it is derived as:

$$\tilde{u}_{j,k}^{h}(\boldsymbol{r}_{L_i}) = \frac{1}{A_{L_i}} \int_{\Omega_{L_i}} u_{j,k}^{h}(\boldsymbol{r}) \, d\Omega$$

$$= \frac{1}{A_{L_i}} \int_{\Gamma_{L_i}} u_j^{h}(\boldsymbol{r}) n_k \, d\Gamma = \sum_{I=1}^{\mathrm{NP}} b_{Ik}(\boldsymbol{r}_{L_i}) u_{jI},$$

$$b_{Ik}(\boldsymbol{r}_{L_i}) = \frac{1}{A_{L_i}} \int_{\Gamma_{L_i}} \psi_I(\boldsymbol{r}) n_k \, d\Gamma, \quad j = \{1, \cdots, 5\}, \quad k = \{1, 2\}, \qquad (30)$$

where A_{L_i} is the area of the sub-domain, and Γ_{L_i} is the boundary of the sub-domain. The five-point Gauss quadrature rule is employed to numerically integrate $b_{Ik}(\boldsymbol{r}_K)$ in Eq. (29) and $b_{Ik}(\boldsymbol{r}_{L_i})$ in Eq. (30).

When analyzing the non-derivative components, $e.g.$, the displacement components, a smoothing operation is performed. The thirteen-point Gauss quadrature rule is used to numerically integrate each sub-domain. The displacement component u_j is smoothed in a cell in terms of the M-th node in Fig. 2(b), as:

$$\tilde{u}_j^{h}(\boldsymbol{r}_M) = \sum_{i=1}^{\mathrm{N_{tri}}} \int_{\Omega_{M_i}} \frac{1}{A_{M_i}} u_j^{h}(\boldsymbol{r}) \, d\Omega$$

$$= \sum_{i=1}^{\mathrm{N_{tri}}} \sum_{I=1}^{\mathrm{NP}} \int_{\Omega_{M_i}} \frac{1}{A_{M_i}} \psi_I(\boldsymbol{r}) u_{jI} \, d\Omega, \quad j = \{1, \cdots, 5\}. \qquad (31)$$

12

By introducing the displacement-strain relationship in Eq. (17) and the constitutive equation in Eq. (24) into the virtual work principle, the linear simultaneous equation is obtained as:

$$\boldsymbol{K}\boldsymbol{U} = \boldsymbol{f}, \tag{32}$$

where $\boldsymbol{K}$ is the stiffness matrix, and $\boldsymbol{f}$ is the force vector. $\boldsymbol{K}$ and $\boldsymbol{f}$ are represented as:

$$\boldsymbol{K} = \int_{\Omega} \boldsymbol{B}^T \boldsymbol{C} \boldsymbol{B} \, d\Omega, \quad \boldsymbol{f} = \int_{\Gamma_t} \boldsymbol{\Psi}^T \bar{\boldsymbol{t}} \, d\Gamma, \tag{33}$$

where the domain $d\Omega$ is derived by the scalar triple product of the covariant base vector, i.e., $d\Omega = [\boldsymbol{G}_1 \boldsymbol{G}_2 \boldsymbol{G}_3] dr^1 dr^2 dr^3$. Although the numerical integration along the plate thickness direction can be analytically carried out, the Newton-Cotes formula is adopted in the numerical integration along the through-thickness direction.

3. Evaluation of fracture mechanics parameters

3.1. Contour integral

If a thin-walled structure includes a through crack and the crack face contact is ignored, the membrane and bending intensity factors can be defined [63,64]. For curved shell structures, e.g., pressure vessels and cylindrical walls, most loads are transferred to the structure as in-plane stress. Two membrane intensity factors K_I and K_{II} are dominant. A schematic illustration of the two deformation modes is presented in Fig. 3(a) and (b).

In the present study, the SRIFs are evaluated by the contour integral using stress resultants. The contour integral is originally formulated for the 2D plane strain/plane stress conditions [65] as shown in Fig. 3(c) and extended to flat shell problems [36,56]. Additionally, the mixed-mode SRIFs are evaluated using the decomposition method [54,61,62], and the contour integral is discretized using the RKs and SSCI [53-56]. The approach is further extended to cracked curved shell problems.

The membrane J-integral value J_1 can be decomposed as:

$$J_1 = J_1^{\text{S}} + J_1^{\text{AS}}, \tag{34}$$
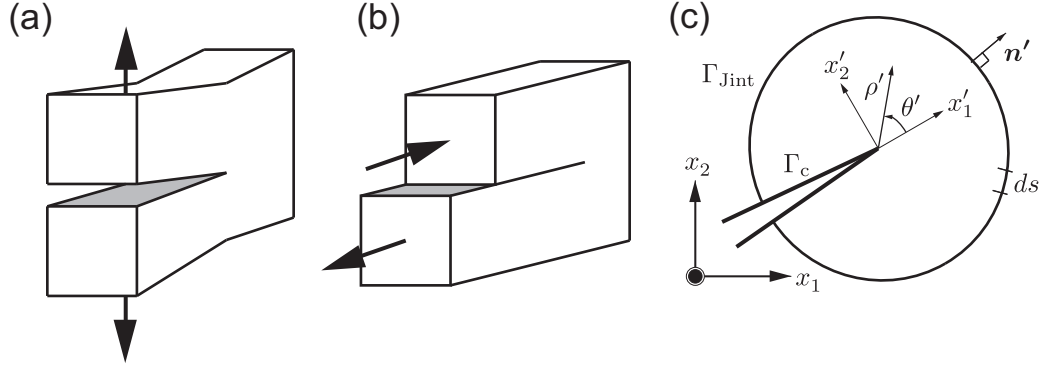
Figure 3: Membrane intensity factors corresponding to deformation modes of cracked body and contour integral. [(a) K_I, (b) K_{II}, (c) contour integral path].

where J_1^{S} and J_1^{AS} are symmetric and asymmetric components, respectively, and the relationships are expressed as:

$$J_1^{\mathrm{S}} = \frac{K_I^2}{E}, \quad J_1^{\mathrm{AS}} = \frac{K_{II}^2}{E},\tag{35}$$

where K_I and K_{II} are the mode-I and -II membrane SRIFs.

The contour J-integral can be expressed on the local coordinate system at the crack tip, as:

$$J_1^k = \int_{\Gamma_{\mathrm{Jint}}} \frac{1}{t_{\mathrm{h}}} \left(W'^k n_1' - N_{ij}'^k \frac{\partial u_i'^k}{\partial x_1'} n_j' \right) d\Gamma$$

$$W'^k = \int_0^{\varepsilon'^k} N_{ij}'^k d\varepsilon_{ij}'^k, \quad N_{ij}'^k = \int_{-t_{\mathrm{h}}/2}^{t_{\mathrm{h}}/2} \sigma_{ij}'^k dx_3',\tag{36}$$

where k=S and AS represent symmetric and asymmetric components, respectively. $(\ )'$ denotes the physical values evaluated using the local coordinate system at the crack tip. Γ_{Jint} is a contour surrounding the crack tip. n_j' is the components of the normal vector. W'^k is the strain energy density. $N_{ij}'^k$ is the stress resultants in terms of membrane forces. dx_3' is the shell thickness direction.

3.2. Coordinate transformation of physical values on curved surface

Previous studies have evaluated the SIFs in cracked curved shells by taking a small contour around the crack tip and assumed that the area within

the small contour is approximately flat [36-39]. In the references [37,38], the assumption that the upper and lower crack faces of shells are orthogonal to the crack front is defined for the domain form of the J-integral. According to the assumption, the small domain is considered to evaluate the J-integral. Hence, this study adopts the abovementioned assumption to evaluate the SRIFs.
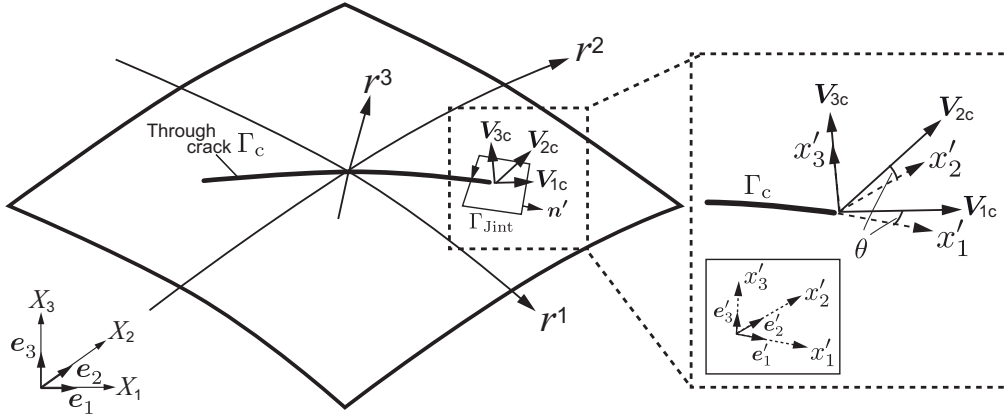
Figure 4: Global and local coordinate systems of curved surface.

The contour integral in Eq. (36) is used by taking a contour Γ_{Jint} on the cracked curved surface. The curved surface that embedded a through crack is shown in Fig. 4. The orthogonal unit vector of the local coordinate system is denoted as $\boldsymbol{V}_{ic}$ (i=1,2,3). The local crack tip coordinate is denoted as $\boldsymbol{x}'$=(x'_1, x'_2, x'_3), and its unit vector is $\boldsymbol{e}'_i$. The physical values based on the local crack tip coordinate system are employed to analyze the contour integral in Eq. (36). The smoothed stress tensor $\tilde{\boldsymbol{\sigma}}'$ on the local crack tip coordinate system can be written as:

$$\tilde{\boldsymbol{\sigma}}' = \boldsymbol{P} \cdot \tilde{\boldsymbol{\sigma}} \cdot \boldsymbol{P}^T, \tag{37}$$

$$\boldsymbol{P} = \begin{bmatrix} \boldsymbol{e}'_1 \cdot \boldsymbol{G}_1 & \boldsymbol{e}'_1 \cdot \boldsymbol{G}_1 & \boldsymbol{e}'_1 \cdot \boldsymbol{G}_1 \\ \boldsymbol{e}'_2 \cdot \boldsymbol{G}_2 & \boldsymbol{e}'_2 \cdot \boldsymbol{G}_2 & \boldsymbol{e}'_2 \cdot \boldsymbol{G}_2 \\ \boldsymbol{e}'_3 \cdot \boldsymbol{G}_3 & \boldsymbol{e}'_3 \cdot \boldsymbol{G}_3 & \boldsymbol{e}'_3 \cdot \boldsymbol{G}_3 \end{bmatrix}. \tag{38}$$

where $\boldsymbol{P}$ is the transformation matrix.

The smoothed strain tensor $\tilde{\boldsymbol{\varepsilon}}'$ on the local crack tip coordinate system can be written as:

$$\tilde{\boldsymbol{\varepsilon}}' = \boldsymbol{Q} \cdot \tilde{\boldsymbol{\varepsilon}} \cdot \boldsymbol{Q}^T, \tag{39}$$

15

$$\boldsymbol{Q} = \begin{bmatrix} \boldsymbol{e}_1' \cdot \boldsymbol{G}^1 & \boldsymbol{e}_1' \cdot \boldsymbol{G}^1 & \boldsymbol{e}_1' \cdot \boldsymbol{G}^1 \\ \boldsymbol{e}_2' \cdot \boldsymbol{G}^2 & \boldsymbol{e}_2' \cdot \boldsymbol{G}^2 & \boldsymbol{e}_2' \cdot \boldsymbol{G}^2 \\ \boldsymbol{e}_3' \cdot \boldsymbol{G}^3 & \boldsymbol{e}_3' \cdot \boldsymbol{G}^3 & \boldsymbol{e}_3' \cdot \boldsymbol{G}^3 \end{bmatrix}, \tag{40}$$

where $\boldsymbol{Q}$ is the transformation matrix.

The normal vector and the derivative of the smoothed displacement also need to define on the local crack tip coordinate system. The relationship of the normal vector between the local crack tip coordinate $\boldsymbol{n}'(=\{n_1', \ n_2'\}^T)$ and the global coordinate $\boldsymbol{n}(=\{n_1, \ n_2\}^T)$ is written as:

$$\boldsymbol{n}' = \boldsymbol{R} \cdot \boldsymbol{n}. \tag{41}$$

Additionally, the relationship of the derivative of the smoothed displacement vectors is expressed as:

$$\frac{\partial \tilde{u}_i'}{\partial x_j'} = \boldsymbol{R} \cdot \begin{bmatrix} \frac{\partial \tilde{u}_1}{\partial r^1} & \frac{\partial \tilde{u}_1}{\partial r^2} \\ \frac{\partial \tilde{u}_2}{\partial r^1} & \frac{\partial \tilde{u}_2}{\partial r^2} \end{bmatrix} \cdot \boldsymbol{R}^T, \tag{42}$$

where $\boldsymbol{R}$ is the transformation matrix. It can be represented as:

$$\boldsymbol{R} = \begin{bmatrix} \boldsymbol{e}_1' \cdot \boldsymbol{e}_1 & \boldsymbol{e}_1' \cdot \boldsymbol{e}_1 \\ \boldsymbol{e}_2' \cdot \boldsymbol{e}_2 & \boldsymbol{e}_2' \cdot \boldsymbol{e}_2 \end{bmatrix}. \tag{43}$$
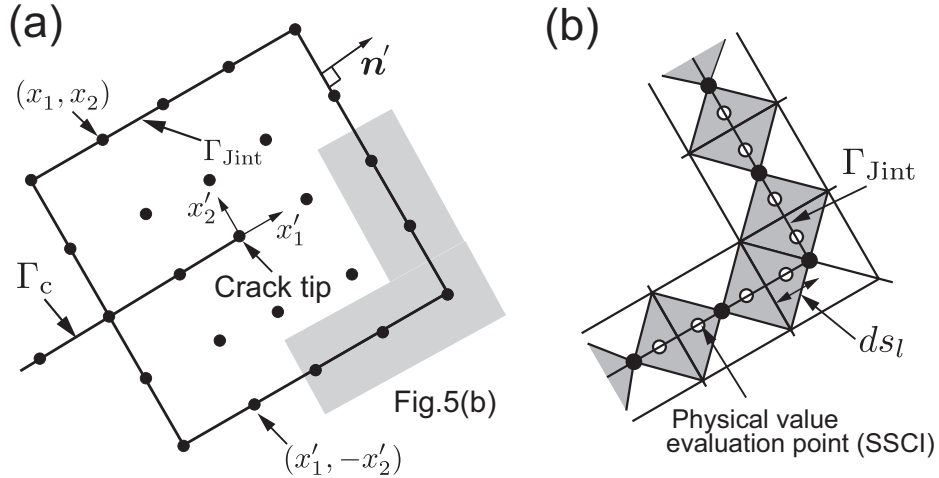
Figure 5: Discretization of contour integral. [(a) contour in meshfree modeling, (b) SSCI discretization].

16

3.3. Discretization of contour integral and mode separation

The contour integral in Eq. (36) is discretized using SSCI, and the Newton-Cotes formula is employed to evaluate $N_{ij}^{\prime k}$. A contour in the mesh-free modeling is shown in Fig. 5(a). Notably, the contour is developed by connecting the nodes surrounding the crack tip. SSCI is employed to discretize the contour integral as shown in Fig. 5(b), and it can be written as:

$$\tilde{J}_1^k = \sum_{l=1}^{\text{Ncell}} \frac{1}{t_{\text{h}}} \left(\tilde{W}^{\prime k} n_1^{\prime} - \tilde{N}_{ij}^{\prime k} \frac{\partial \tilde{u}_i^{\prime k}}{\partial x_1^{\prime}} n_j^{\prime} \right)_l ds_l, \quad \tilde{W}^{\prime} = \frac{1}{2} \tilde{N}_{ij}^{\prime k} \tilde{\varepsilon}_{ij}^{\prime}, \qquad (44)$$

where Ncell is the number of triangular domains along the contour. $N_{ij}^{\prime k}$ and $u_i^{\prime k}$ are evaluated at points $(x_1^{\prime}, x_2^{\prime})$ and $(x_1^{\prime}, -x_2^{\prime})$ as shown in Fig. 5(a). The position of the two points is symmetrical across the crack segment. The stress resultants $\boldsymbol{N}^k(x_1^{\prime}, x_2^{\prime})$ and displacements $\boldsymbol{u}^k(x_1^{\prime}, x_2^{\prime})$ for symmetric and asymmetric components can be written as:

$$\boldsymbol{N}^{\prime \text{S}}(x_1^{\prime}, x_2^{\prime}) = \frac{1}{2} \left\{ \begin{array}{c} N_{11}^{\prime}(x_1^{\prime}, x_2^{\prime}) + N_{11}^{\prime}(x_1^{\prime}, -x_2^{\prime}) \\ N_{22}^{\prime}(x_1^{\prime}, x_2^{\prime}) + N_{22}^{\prime}(x_1^{\prime}, -x_2^{\prime}) \\ N_{12}^{\prime}(x_1^{\prime}, x_2^{\prime}) - N_{12}^{\prime}(x_1^{\prime}, -x_2^{\prime}) \end{array} \right\}, \qquad (45)$$

$$\boldsymbol{N}^{\prime \text{AS}}(x_1^{\prime}, x_2^{\prime}) = \frac{1}{2} \left\{ \begin{array}{c} N_{11}^{\prime}(x_1^{\prime}, x_2^{\prime}) - N_{11}^{\prime}(x_1^{\prime}, -x_2^{\prime}) \\ N_{22}^{\prime}(x_1^{\prime}, x_2^{\prime}) - N_{22}^{\prime}(x_1^{\prime}, -x_2^{\prime}) \\ N_{12}^{\prime}(x_1^{\prime}, x_2^{\prime}) + N_{12}^{\prime}(x_1^{\prime}, -x_2^{\prime}) \end{array} \right\}, \qquad (46)$$

$$\boldsymbol{u}^{\prime \text{S}}(x_1^{\prime}, x_2^{\prime}) = \frac{1}{2} \left\{ \begin{array}{c} u_1^{\prime}(x_1^{\prime}, x_2^{\prime}) + u_1^{\prime}(x_1^{\prime}, -x_2^{\prime}) \\ u_2^{\prime}(x_1^{\prime}, x_2^{\prime}) - u_2^{\prime}(x_1^{\prime}, -x_2^{\prime}) \end{array} \right\}, \qquad (47)$$

$$\boldsymbol{u}^{\prime \text{AS}}(x_1^{\prime}, x_2^{\prime}) = \frac{1}{2} \left\{ \begin{array}{c} u_1^{\prime}(x_1^{\prime}, x_2^{\prime}) - u_1^{\prime}(x_1^{\prime}, -x_2^{\prime}) \\ u_2^{\prime}(x_1^{\prime}, x_2^{\prime}) + u_2^{\prime}(x_1^{\prime}, -x_2^{\prime}) \end{array} \right\}. \qquad (48)$$

The components of $\boldsymbol{N}^{\prime k}(x_1^{\prime}, x_2^{\prime})$ and $\boldsymbol{u}^{\prime k}(x_1^{\prime}, x_2^{\prime})$ are employed in Eq. (44) to obtain the J-integral value.

4. Numerical examples

Several numerical examples are presented for analyzing the fracture mechanics parameters in cracked curved shells. First, the cracked shallow shells are analyzed, and the model is extended to consider the cracked cylinders. Additionally, the J-integral value and mixed-mode SRIFs are evaluated. Furthermore, the simplified fatigue crack propagation simulation is carried out.

The calculated results are compared with the reference solutions. The J-integral value is evaluated using Eq. (44), and the value is transformed to the mode-I and -II SRIFs using the decomposition method. To investigate the accuracy in the fracture mechanics parameters, the error is defined as:

$$error = \frac{|K^{\text{Mfree.}} - K^{\text{Ref.}}|}{K^{\text{Ref.}}} \times 100 \ \ [\%], \tag{49}$$

where $K^{\text{Mfree.}}$ and $K^{\text{Ref.}}$ are the SRIFs obtained using the meshfree method and reference solutions, respectively.
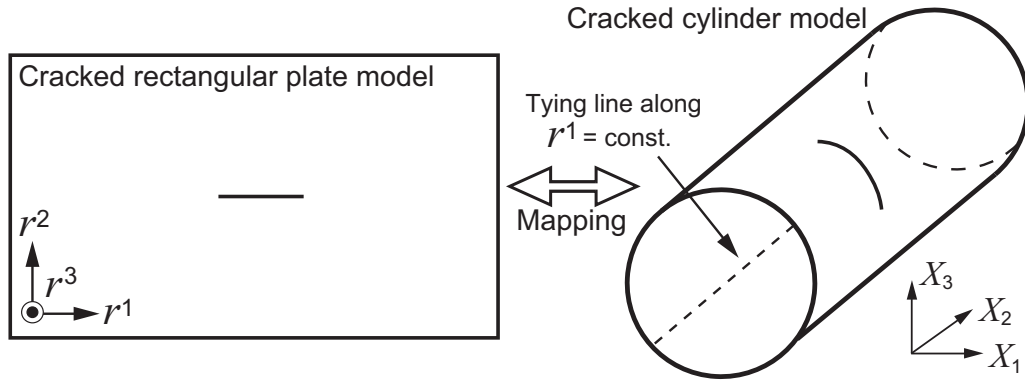
Figure 6: Meshfree modeling of cracked cylinder using mapping technique.

In the meshfree modeling, the curvilinear geometry of curved and cylindrical shells is developed from a flat meshfree model using the mapping technique. A schematic illustration of a cracked cylinder model is shown in Fig. 6. The mapping technique improves the efficiency in the procedure of creating analysis models. All DOFs of the overlapped nodes along both ends, e.g., r^1=const., are tied by employing SKs. However, the SKs only satisfy the Kronecker delta property on the nodes, which may lead to an incompatible approximation and reduce the accuracy of the meshfree approximation. Previous studies have attempted to overcome this problem [66,67]. In the present study, more than 60 nodes are employed along the connecting edge, and the crack is modeled on the opposite side. These techniques are applied to reduce the numerical error caused by the incompatible approximation.

4.1. Shallow shell with axial crack under uniform pressure

A shallow shell including an axial through crack under uniform pressure is analyzed. The model is shown in Fig. 7. The arc length L_1 and the

longitudinal length L_2 are 2.0 [m]. The curved shell radius and half crack length are denoted as R and a, respectively. The thickness t_h is 0.05 [m]. Uniform pressure of p=1.0 [MPa] is applied throughout the curved shell, and four edges are clamped. Here, K_I is investigated by changing half crack length a (=0.2, 0.3, 0.4, and 0.5 [m]) and curvature radius R (=5.0, 6.66, 10.0, 13.33, 20.0, and 40.0 [m]). E=210,000 [MPa] and ν=0.3 are chosen.
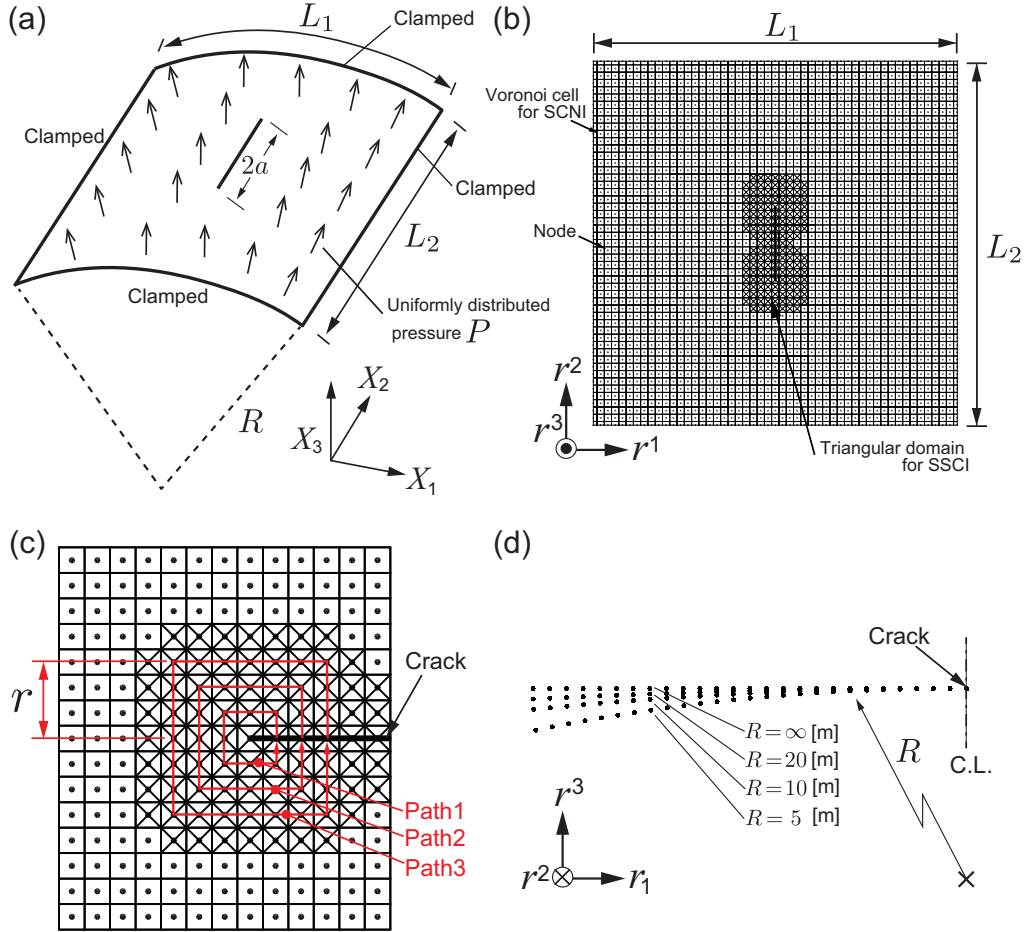
Figure 7: Shallow shell with axial crack under uniform pressure. [(a) analysis model to be solved, (b) original meshfree model for 51×51 nodes, a=0.2 [m], (c) J-integral contours for fracture mechanics analysis, (d) mapped meshfree models for R=5.0, 10.0, 20.0 and ∞ [m] (51×51 nodes)].

First, a meshfree model for the intact rectangular flat shell is developed. A through crack is introduced into the meshfree model. The flat meshfree

19

model maps onto the curved surface to generate a cracked shallow shell model. Four meshfree models are arranged with 11×11, 26×26, 51×51, and 101×101 uniformly distributed nodes. The original meshfree model with 51×51 nodes for a=0.2 [m] is shown in Fig. 7(b). The entire domain is discretized using Voronoi cells and the triangular sub-domains divided from Voronoi cells are employed around the crack. The enlarged view of the meshfree model around the crack is shown in Fig. 7(c). Rectangular contours are set for the fracture mechanics parameter evaluation, as follows: Path1, Path2, and ··· around the crack tip. Here, r is the half length of contours. The cross-section of the mapped meshfree models are shown in Fig. 7(d), including R=5.0, 10.0, and 20.0 [m]. As a reference, the flat shell model (R=∞ [m]) is also presented.

The fracture mechanics option in ABAQUS [68] is applied as reference solutions. The FEM model for R=5.0 [m] and a=0.2 [m] is shown in Fig. 8(a). The crack tip is surrounded using three-node triangular shell elements (element type: S3), and the remaining area is meshed using four-node quadrilateral shell elements (element type: S4R). Throughout the domain, the element size is approximately 0.05 [m], and the element size around the crack tip is approximately 0.1 [mm]. For the SRIF evaluation, the values of Path2 is taken.
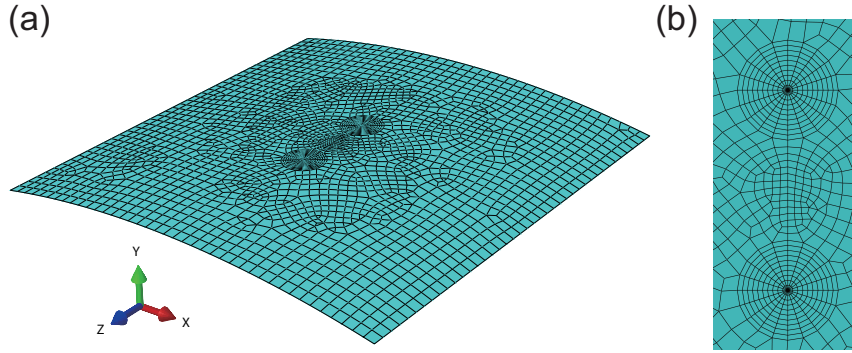
Figure 8: (a) FEM model of cracked shallow shell for R=5.0 [m] and a=0.2 [m], (b) enlarged view around crack.

For different contour sizes, K_I is investigated with various curved shell radius. R is changed using the mapping technique. The results are shown in Fig. 9(a). The contours from Path2 to Path5 are employed. As the contour size increases, the error in K_I uniformly increases. Meanwhile, the error becomes larger as the radius decreases. It is found that the error in

Path2 is less than 1.0% even for R=5.0 [m]. Moreover, K_I is investigated for different crack lengths with various node spacings. The results are presented in Fig. 9(b). Path2 is taken for all cases. As the node spacing decreases, the error in K_I monotonically decreases for different crack lengths. Notably, the node spacing for a=0.2 [m] in the meshfree model with 51×51 nodes is approximately d_I=0.04 [m], *i.e.*, a/d_I=5. The error in K_I is less than 1.0 [%] as a/d_I is greater than 5.0.
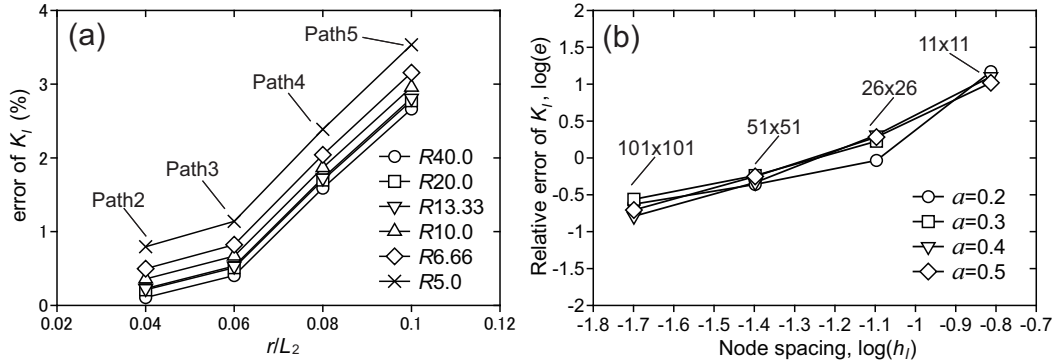
Figure 9: Accuracy investigation in K_I [(a) error assessment in K_I with various curved shell integral contours and radii for 51×51 nodes, (b) error assessment in K_I with various node spacings and crack lengths for Path2 contour].

Next, K_I is investigated for different half crack lengths of a=0.2, 0.3, 0.4, and 0.5 [m]. The calculated results are shown in Fig. 10(a). The meshfree model with 51×51 nodes is employed, and Path2 is chosen. The reference solution obtained from the FEM is adopted. The results show that the value of K_I increases as the crack length increases. The meshfree results are in good agreement with the FEM results. Additionally, K_I is investigated for different radii of R=5.0, 6.66, 10.0, 13.33, 20.0, and 40.0 [m]. The results are shown in Fig. 10(b). In the figure, the horizontal axis represents the curvature, *i.e.*, κ=1/R. After taking the highest value of K_I at approximately κ=0.05 [m], K_I monotonically decreases as the curvature increases. It is confirmed that the SRIF evaluation using the proposed meshfree method has good agreement with the reference solutions for different crack lengths and different curvatures.

4.2. Shallow shell with inclined crack under tensile load

A shallow shell including an inclined crack under tensile load is calculated. The model is shown in Fig. 11(a). R=5.0 [m] is chosen. The model sizes

21
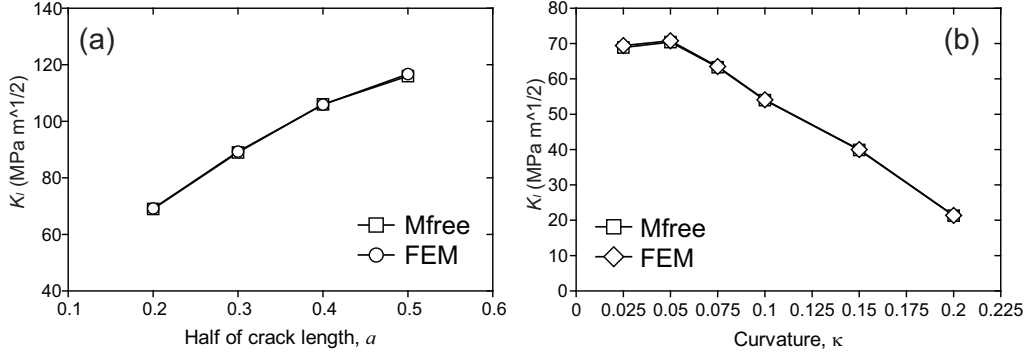
Figure 10: Mode-I SRIF for shallow shells with axial crack. [(a) K_I results with various crack lengths for R=5.0 [m], (b) K_I results with various curvatures for a=0.2 [m]].

and material parameters are the same as the previous example. Tensile loads of p=1.0 [MPa] are applied to both sides of the shallow shell. This problem is analyzed by changing half crack length a and inclined crack angle β. Calculations are carried out with a=0.2, 0.3, 0.4, and 0.5 [m] for β=0, 30, 45, 60, and 90 [deg.]. The FEM results are employed as the reference solutions. The original meshfree model for a=0.4 [m] and β=30 [deg.] is shown in Fig. 11(b). Around the crack, the nodes are uniformly distributed, and the node spacing is approximately d_I=0.025 [m].

K_I and K_{II} are analyzed, and the results are shown in Fig. 12(a) and (b), respectively. From the comparison, the meshfree results have good accuracy not only for K_I but also for K_{II}. When β is small, K_I is dominant and the value monotonically decreases to zero at β=90 [deg.]. While K_{II} is zero at β=0 [deg.], it gradually increases up to 45 [deg.]. When β is larger than 45 [deg.], K_I monotonically decreases and becomes zero at 90 [deg.]. For all cases, the results obtained from the meshfree method agree well with the FEM results. This indicates that the mixed-mode problems can be positively simulated using the proposed meshfree method and the mode separation technique.

4.3. Cylindrical shell with axial crack under uniform internal pressure

A cylindrical shell including an axial through crack under uniform internal pressure is analyzed. In this example, the same settings with the reference solutions are considered for the geometry scantlings and material properties. The geometry and BCs are shown in Fig. 13(a). The length L_1, radius R, and thickness t_h are 100 [mm], 20 [mm], and 0.25 [mm], respectively.
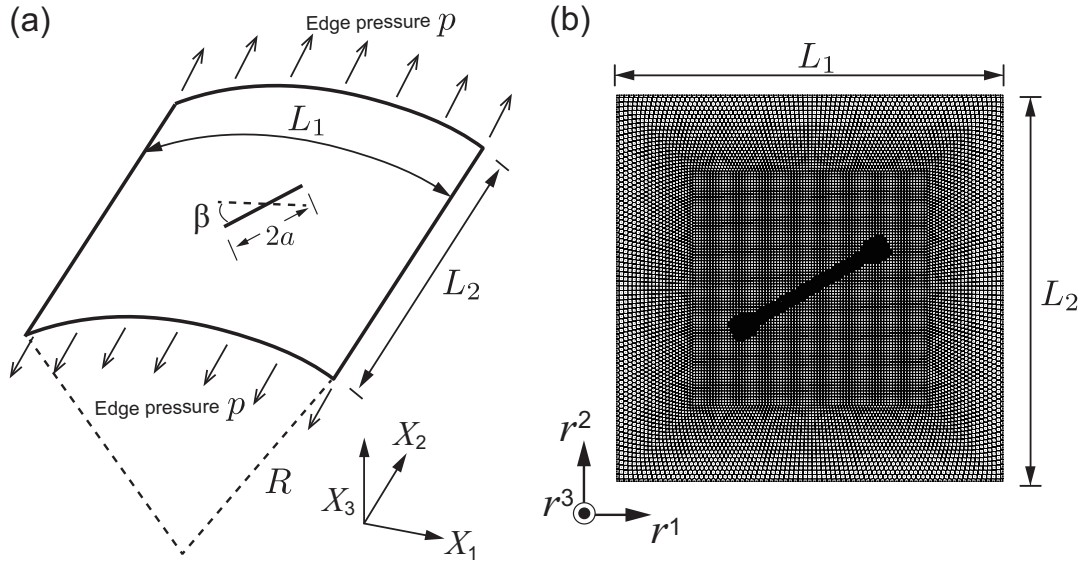
Figure 11: Shallow shell with inclined crack under tensile load. [(a) analysis model to be solved, (b) original meshfree model for a=0.4 [m] and β=30 [deg.]].
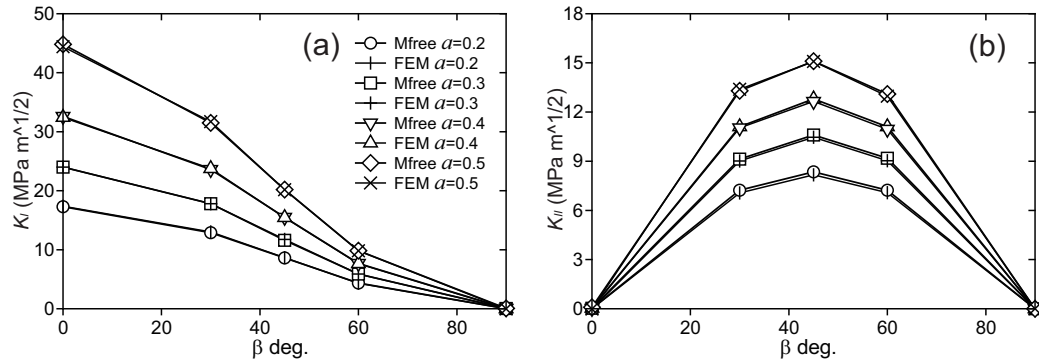
Figure 12: Mixed-mode SRIFs for shallow shells with inclined crack. [(a) K_I with various β, (b) K_{II} with various β].

23

Uniform pressure of p=1.0 [MPa] is applied throughout the internal surface of the cylinder. Three cases of different crack lengths are calculated: a=4.92, 7.38, and 9.841 [mm]. E=1,000 [MPa] and ν=0.3 are chosen. The original meshfree model for a=4.92 [mm] is shown in Fig. 13(b). The node spacing around the crack is d_I=0.7 [mm]. The mapped meshfree model is shown in Fig. 14(a). Tying is employed to join two edges (r^1=const.) of the original meshfree model. The FEM model is shown in Fig. 14(b). The element size throughout the domain is approximately 1.0 [mm]. Around the crack tip, the element size is 0.1 [mm]. The meshfree results are compared with the FEM results and the results from reference studies [37,69]. This problem is a pure mode-I case.
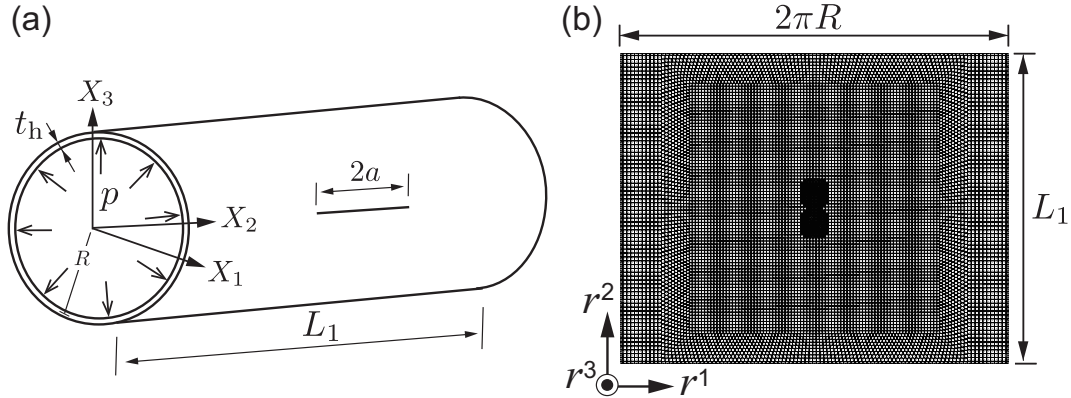
Figure 13: Cylindrical shell with axial crack under internal pressure. [(a) analysis model to be solved, (b) original meshfree model for a=4.92 [mm]].

The J-integral values J_1^{S} and K_I are investigated for different crack lengths. The meshfree results for J_1^{S} are presented in Fig. 15(a) and compared with the FEM results. The meshfree results for K_I are presented in Fig. 15(b) and compared with the analytical solution [69] and the numerical results obtained using the Phantom node method [37]. As the crack length increases, the J_1^{S} and K_I monotonically increase. The results of the proposed meshfree method agree well with the results obtained from the FEM and reference studies.

4.4. Cylindrical shell with circumferential crack under tensile load

A cylindrical shell including a circumferential through crack shown in Fig. 16(a) is considered. Tensile load is applied along the longitudinal direction.

24
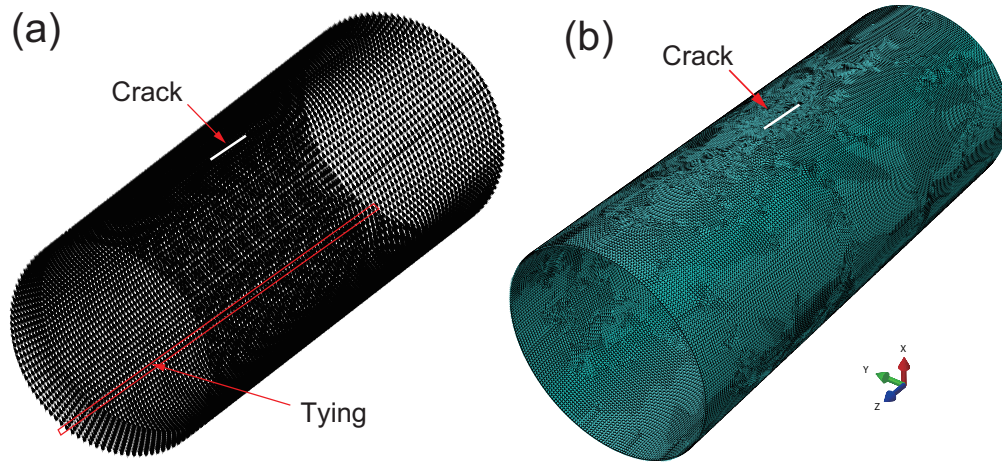
Figure 14: Cylindrical shell model for a=4.92 [mm]. [(a) mapped meshfree model, (b) FEM model].
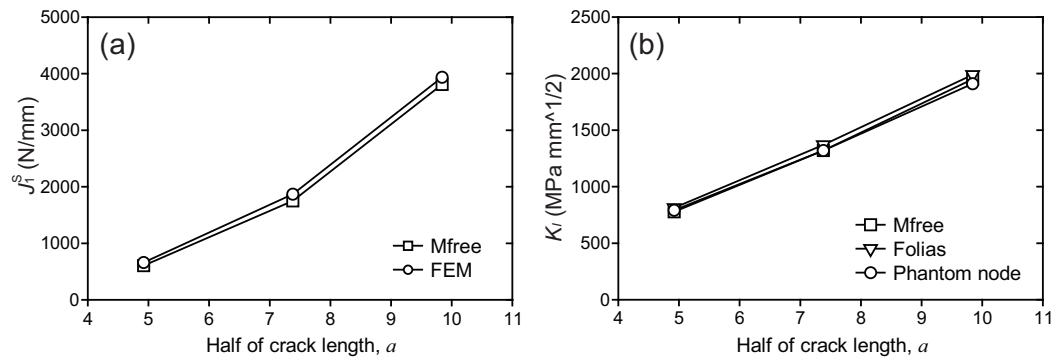
Figure 15: Fracture parameters for cylindrical shell with axial crack. [(a) J_1^S with various crack lengths, (b) K_I with various crack lengths].

The radius R is 25.0 [mm], and the length L_1 is 120.0 [mm]. The shell thickness t_h is 1.0 [mm]. Tensile load of $P=2\pi R\sigma_{nom}t_h$ is applied to both ends of the cylinder, and the nominal axial stress σ_{nom} is 1.0 [MPa]. Six different crack lengths are considered. The circumferential crack length is $2a=2\theta R$, and 2θ vary from 10 to 60 [degs.]. $E=210,000$ [MPa] and $\nu=0.3$. The node spacing of the meshfree model around the crack is $d_I=1.15$ [mm]. This problem is a pure mode-I case.
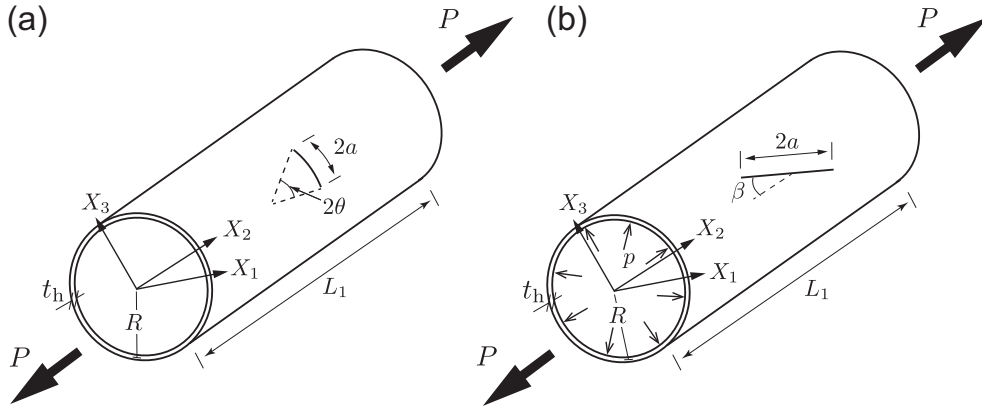
Figure 16: Cracked cylindrical shells to be solved. [(a) cylindrical shell with circumferential crack under tensile load, (b) cylindrical shell with inclined crack under tensile load and internal pressure].

The stress distribution σ^{22} of the meshfree and FEM methods for $2\theta=30$ [deg.] are shown in Fig. 17(a) and (b), respectively. Nearly the same stress distribution can be obtained from both numerical methods. The stress concentration can be observed around the crack tip. Next, K_I is analyzed, and the results are compared with the FEM results. The results are shown in Fig. 18. As can be seen, K_I increases with the crack length. The results obtained using the meshfree method are in good agreement with the FEM results up to $2\theta=40$ [deg.]. However, differences emerge as the crack length becomes large. Xing *et al.* [39] reports a bulging phenomenon occurring around the crack tip when the crack length is relatively large. It means that local deformation around the crack strongly affects the fracture mechanics parameter evaluation.

26
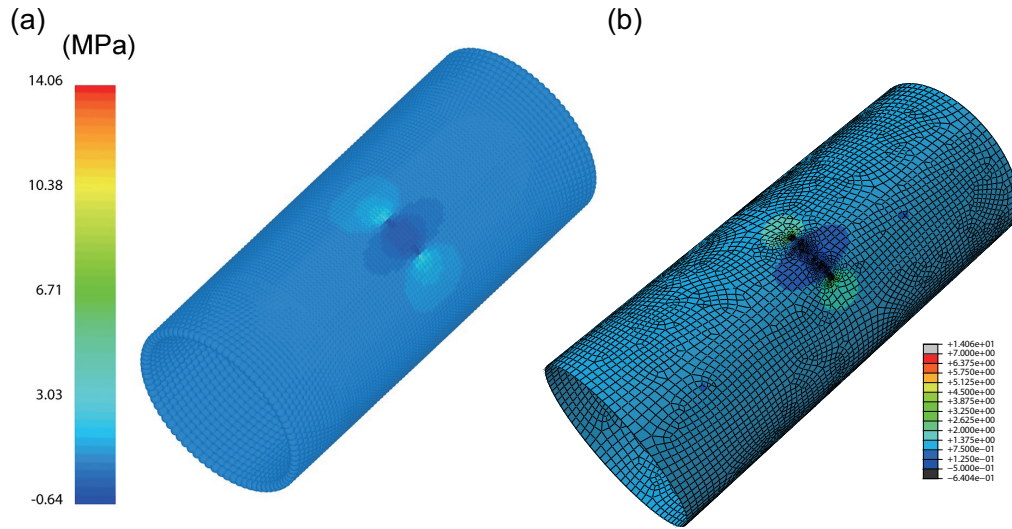
Figure 17: Stress distribution σ^{22} for 2θ=30 [deg.]. [(a) meshfree model, (b) FEM model].
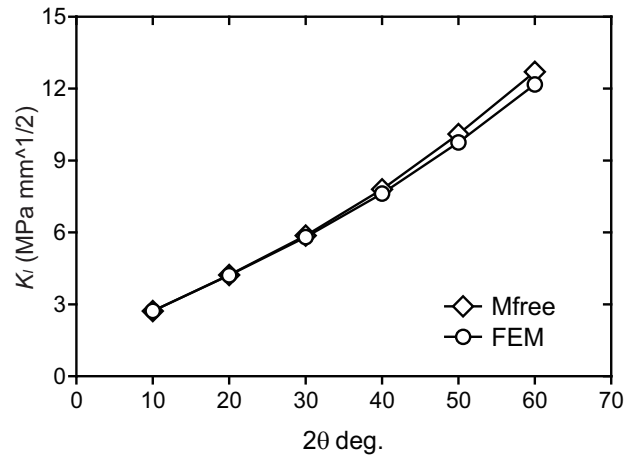
Figure 18: Mode-I SRIF for cylindrical shell with circumferential crack with various crack lengths [m].

4.5. Cylindrical shell including inclined crack under tensile load and uniform internal pressure

A cylindrical shell including an inclined crack shown in Fig. 16(b) is analyzed. Tensile load is applied to both edges of the cylinder, and uniform internal pressure is also employed. The cylinder dimensions and material properties are the same as Section 4.4. A through crack a=8.727 [mm] is introduced, and the crack is inclined for β=0, 30, 45, 60, and 90 [deg.]. Axial tensile loads of P=$2\pi R\sigma_{\mathrm{nom}}t_{\mathrm{h}}$ (σ_{nom}=1.0 [MPa]), and uniform internal pressure of p=1.0 [MPa] are applied. This is a mixed-mode problem.

Similarly, the stress distribution σ^{22} of the meshfree and FEM models for β=45 [deg.] are shown in Fig. 19(a) and (b), respectively. As the previous example, nearly the same stress distribution around the crack can be captured, and the stress distribution for the mixed-mode phenomenon is obtained from both numerical methods.

The J-integral value and mixed-mode SRIFs are investigated. The SRIFs are separated from J_1 using the decomposition method. The results for J_1 is shown in Fig. 20. The J_1 value monotonically increases as β becomes larger. The results for K_I and K_{II} are shown in Fig. 21(a) and (b), respectively. K_I is increases as β becomes larger. Additionally, K_{II} is almost zero at 0 and 90 [degs.] and has a non-zero value between 0 and 90 [degs.]. The meshfree results have good agreement with the FEM results. Therefore, it is confirmed that the proposed numerical methods are effective in analyzing the fracture mechanics problems for cracked cylinders.

4.6. Simplified fatigue crack propagation analysis for cylindrical shell

A fatigue crack propagation analysis is carried out for a cylindrical shell with a circumferential crack. The fatigue crack propagation model is presented in Fig. 16(a). A small scale yielding condition is assumed, and the crack propagation is analyzed according to Paris' law. The cylinder dimensions and material properties are the same as Section 4.4. It is assumed that the cylindrical shell is subjected to cyclic tensile loads, and the stress ratio is equal to zero. The maximum tensile stress σ_{nom} is 150 [MPa]. The circumferential crack length is defined as $2a$=$2\theta R$ [m], and the initial 2θ is 10 [deg.]. The coefficients of the fatigue crack propagation analysis are C=1.64755$\times10^{-11}$ and m=3 [70]. The standard Paris' law, $i.e.$, da/dN=$C\Delta K^m$ is adopted. The units of da/dN and ΔK are [m/cycle] and [MPa$\sqrt{\mathrm{m}}$], respectively. During the crack propagation simulation, the constant crack length increment Δa=0.0005 [m] is taken.
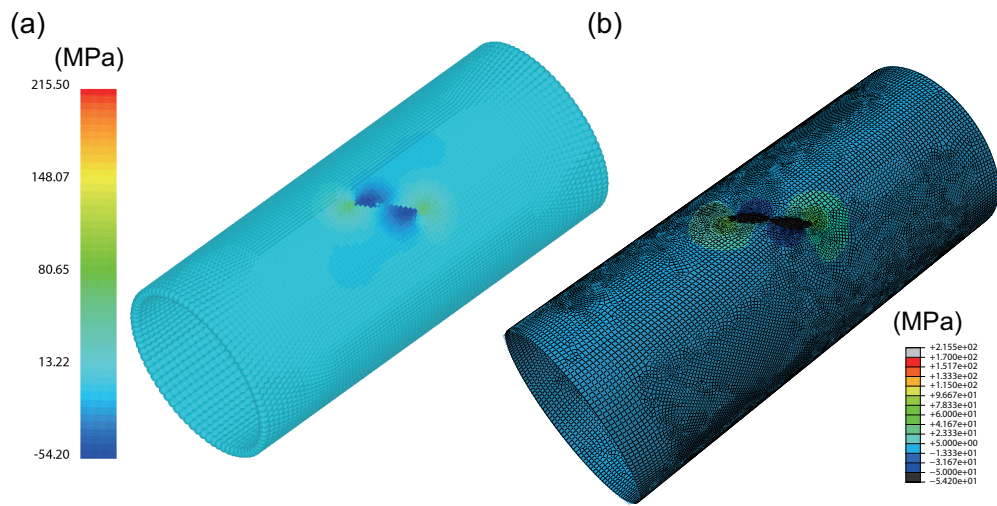
Figure 19: Stress distribution σ^{22} for $\beta=45$ [deg.]. [(a) meshfree model, (b) FEM model].
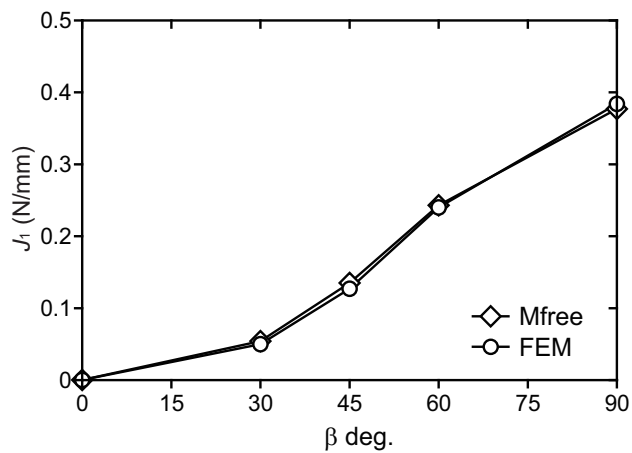
Figure 20: J_1 value for cylindrical shell with inclined crack with various β [deg.].
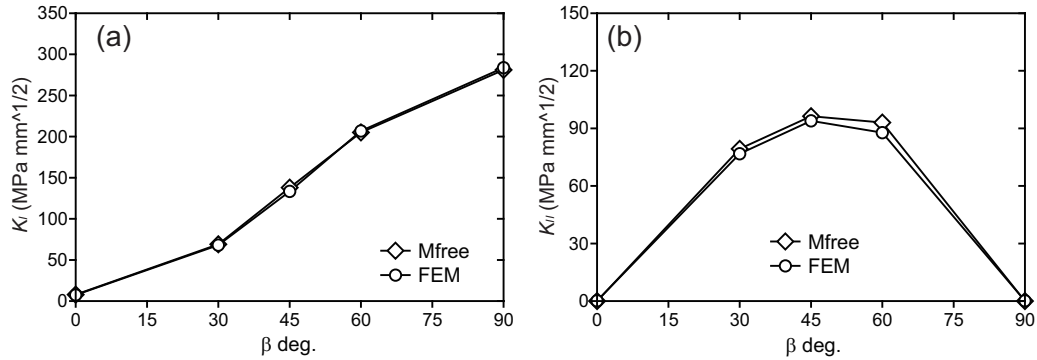
Figure 21: Mixed-mode SRIFs for cylindrical shell with inclined crack. [(a) K_I with various β [deg.], (b) K_{II} with various β [deg.]].

First, the mode-I SRIF with various crack lengths is evaluated. The SRIF for the specified crack length can be obtained by interpolating on the half crack length - SRIF diagram (a - K_I diagram). In the analysis process, the re-meshing is avoided. Next, ΔK is substituted into Paris' law to obtain the number of cycles with a constant crack increment. The simplified simulation of fatigue crack propagation is carried out using the proposed meshfree method and FEM. The relationship between the crack length and number of loading cycles is presented in Fig. 22. The crack length gradually increases before 40,000 cycles; however, it dramatically increases after 40,000 cycles. Based on the results presented in Fig. 22, it is confirmed that the fatigue crack propagation analysis using the proposed meshfree method is in good agreement with the FEM results.

5. Conclusion

An effective meshfree Galerkin method is proposed for fracture mechanics problems involving curved shell structures. The field variables and arbitrary shell geometry are approximated by the RKs and transferred between the different coordinates using the mapping technique. In the meshfree method, the diffraction method, visibility criterion, and enriched basis are adopted to model the crack segment. The contour integral is employed to analyze the fracture mechanics parameters, and the decomposition method is adopted to extract the mixed-mode SRIFs. Nodal integration techniques, *i.e.*, SCNI and SSCI, are employed to evaluate the stiffness matrix and contour integral.
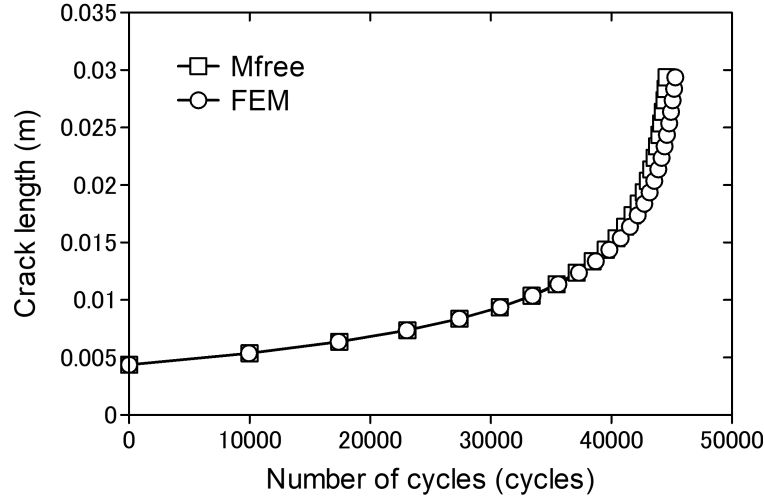
Figure 22: Simplified fatigue crack propagation simulation for cylindrical shell.

Several benchmark examples of curved shells with a through crack are investigated to demonstrate the accuracy of the proposed meshfree method. The results for the J-integral value and mixed-mode SRIFs of the proposed method are compared with reference results obtained from the FEM and other numerical methods. Because the contour integral for curved shell structures lacks path independence, the accuracy in the contour integral is carefully examined by changing the curved shell radius, crack length, and contour integral path. The numerical demonstration revealed that the proposed approach can provide accurate results for the single- and mixed-mode problems compared with the reference solutions. Additionally, the simplified crack propagation simulation for the cracked cylindrical shell is conducted by employing Paris' law.

Although the computational time of RKPM is longer than the conventional FEM, the RKPM has its advantages, particularly with regard to fracture mechanics problems. The proposed method can also be adopted to find numerical solutions for cracked curved shells. The major research objectives of future work are to analyze the complex crack propagations in practical engineering applications and to more efficiently implement the proposed method.

31

Acknowledgements

References

[1] Etube LS. Fatigue and fracture mechanics of offshore structures. Bury St Edmunds; 2001.

[2] Bowness D, Lee MMK. The development of an accurate model for the fatigue assessment of doubly curved cracks in tubular joints. Int J Fract 1995;73:129-47.

[3] Qian X, Nguyen CT, Petchdemaneengam Y, Ou Z, Swaddiwudhipong S, Marshall P. Fatigue performance of tubular X-joints with PJP+welds: II-Numerical investigation. J Constr Steel Res 2013;89:252-61.

[4] Qian X, Dodds Jr. RH, Choo YS. Mode mixity for tubular K-joints with weld toe cracks. Eng Fract Mech 2006;73:1321-42.

[5] Yagi K, Tanaka S, Kawahara T, Nihei K, Okada H, Osawa N. Evaluation of crack propagation behaviors in a T-shaped tubular joint employing tetrahedral FE modeling. Int J Fatigue 2017;96:270-82.

[6] Department of Energy, Great Britain. Offshore Installations : Guidance on Design, Construction and certification. Merseyside; 1984.

[7] Det Norske Veritas. Fatigue design of offshore steel structures, Recommended Practice DNV-RP-C203. Oslo; 2011.

[8] Murakami Y. Stress Intensity Factors Handbook: Vol. 2. Oxford; 1987.

[9] Aliabadi MH, Rooke DP. Numerical Fracture Mechanics, Solid mechanics and its applications. Dordrecht; 1991.

[10] Irwin GR. Analysis of stresses and strains near the end of a crack traversing a plate. J Appl Mech;1957;24:361-64.

[11] Paris PC, Sih GC. Stress analysis of cracks. ASTM STP 381 1965:30-83.

[12] Barsoum RS, Loomis RW, Stewart BD. Analysis of through cracks in cylindrical shells by the quarter-point elements. Int J Fract 1979;15:259-80.

[13] Potyondy DO, Wawrzynek PA, Ingraffea AR. Discrete crack growth analysis methodology for through cracks in pressurized fuselage structures. Int J Numer Meth Eng 1995;38:1611-33.

[14] Hung ND, Ngoc TT. Analysis of cracked plates and shells using metis finite element model. Finite Elem Anal Des 2004;40:855-78.

[15] Furukawa CH, Bucalem ML, Mazella IJG. On the finite element modeling of fatigue crack growth in pressurized cylindrical shells. Int J Fract 2009;31:629-35.

[16] Aliabadi MH. A new generation of boundary element methods in fracture mechanics. Int J Fract 1997;86:91-125.

[17] Belytschko T, Lu YY, Gu L. Element-free Galerkin Methods. Int J Numer Meth Eng 1994;37:229-56.

[18] Liu WK, Jun S, Zhang YF. Reproducing kernel particle methods. Int J Numer Meth Fluid 1995;20:1081-106.

[19] Atluri SN, Zhu T. A new meshless local Petrov-Galerkin (MLPG) approach in computational mechanics. Comput Mech 1998;22:117-27.

[20] Rabczuk T, Areias P. A meshfree thin shell for arbitrary evolving cracks based on an extrinsic basis. Comput Model Eng Sci 2006;16:115-30.

[21] Xu BB, Gau XW, Jiang WW, Cui M, Lv J. Galerkin free element method and its application in fracture mechanics. Eng Fract Mech 2019;218:106575.

[22] Moës N, Dolbow J, Belytschko T. A finite element method for crack growth without remeshing. Int J Numer Meth Eng 1999;46:131-50.

[23] Hughes TJR, Cottrell JA, Bazilevs Y. Isogeometric analysis: CAD, finite elements, NURBS, exact geometry and mesh refinement. Comput Meth Appl Mech Engrg 2005;194:4135-95.

[24] De Luycker E, Benson DJ, Belytschko T, Bazilevs Y, Hsu MC. X-FEM in isogeometric analysis for linear fracture mechanics. Int J Numer Meth Eng 2011;87:541-65.

[25] Tanaka S, Okada H, Okazawa S. A wavelet Galerkin method employing B-spline bases for solid mechanics problems without the use of a fictitious domain. Comput Mech 2012;50:35-48.

[26] Tanaka S, Okada H, Okazawa S, Fujikubo M. Two-dimensional fracture mechanics analyses using the wavelet Galerkin method and extended finite element method. Int J Numer Meth Eng 2013;93:1082-108.

[27] Tanaka S, Suzuki H, Ueda S, Sannomaru S. An extended wavelet Galerkin method with a high-order B-spline for 2D crack problems. Acta Mech 2015;226:2159-75.

[28] Tanaka S, Sannomaru S, Imachi M, Hagihara S, Okazawa S, Okada H. Analysis of dynamic stress concentration problems employing spline-based wavelet Galerkin method. Eng Anal Bound Elem 2015;58:129-39.

[29] Sannomaru S, Tanaka S, Yoshida K, Bui TQ, Okazawa S, Hagihara S. Treatment of Dirichlet-type boundary conditions in the spline-based wavelet Galerkin method employing multiple point constraints. Appl Math Model 2017;43:592-610.

[30] Silling SA. Reformulation of elasticity theory for discontinuities and long-range forces. J Mech Phys Solids 2000;48:175-209.

[31] Silling SA, Askari E. A meshfree method based on the peridynamic model of solid mechanics. Comput Struct 2005;83:1526-35.

[32] Madenci E, Oterkus E. Peridynamic theory and its applications. Springer, New York; 2014.

[33] Imachi M, Tanaka S, Bui TQ. Mixed-mode dynamic stress intensity factors evaluation using ordinary state-based peridynamics. Theor Appl Fract Mech 2018;93:97-104.

[34] Imachi M, Tanaka S, Bui TQ, Oterkus S, Oterkus E. A computational approach based on ordinary state-based peridynamics with new transition bond for dynamic fracture analysis. Eng Fract Mech 2019;206:359-74.

[35] Imachi M, Tanaka S, Ozdemir M, Bui TQ, Oterkus S, Oterkus E. Dynamic crack arrest analysis by ordinary state-based peridynamics. Int J Fract 2020;221:155-169.

[36] Dirgantara T, Aliabadi MH. Dual boundary element formulation for fracture mechanics analysis of shear deformable shells. Int J Solid Struct 2001;38:7769-800.

[37] Chau-Dinh T, Zi G, Lee PS, Song J, Rabczuk T. Phantom-node method for shell models with arbitrary cracks. Comput Struct 2012;92-93:242-56.

[38] Nguyen-Thanh N, Valizadeh N, Nguyen MN, Nguyen-Xuan H, Zhuang X, Areias P, Zi G, Bazilevs Y, De Lorenzis L, Rabczuk T. An extended isogeometric thin shell analysis based on Kirchhoff-Love theory. Comput Methods Appl Mech Eng 2015;284:265-91.

[39] Xing C, Wang Y, Waisman H. Fracture analysis of cracked thin-walled structures using a high-order XFEM and Irwin's integral. Comput Struct 2019;212:1-19.

[40] Wang D, Chen JS. Locking-free stabilized conforming nodal integration for meshfree Mindlin-Reissner plate formulation. Comput Meth Appl Mech Engrg 2004;193:1065-83.

[41] Wang D, Sun Y. A Galerkin meshfree method with stabilized conforming nodal integration for geometrically nonlinear analysis of shear deformable plates. Int J Comput Meth 2011;8:685-703.

[42] Chen JS, Wang HP. New boundary condition treatments in meshfree computation of contact problems. Comput Methods Appl Mech Engrg 2000;187:441-68.

[43] Chen JS, Wu CT, Yoon S, You Y. A stabilized conforming nodal integration for Galerkin meshfree methods. Int J Numer Meth Eng 2001;50:435-66.

[44] Chen JS, Yoon S, Wu CT. Non-linear version of stabilized conforming nodal integration for Galerkin mesh-free methods. Int J Numer Meth Eng 2002:53:2587-615.

[45] Wang D, Chen JS. A Hermite reproducing kernel approximation for thin-plate analysis with sub-domain stabilized conforming integration. Int J Numer Meth Eng 2008;74:368-90.

[46] Wang D, Lin Z. Free vibration analysis of thin plates using Hermite reproducing kernel Galerkin meshfree method with sub-domain stabilized conforming integration. Comput Mech 2010;46:703-19.

[47] Wang D, Lin Z. Dispersion and transient analyses of Hermite reproducing kernel Galerkin meshfree method with sub-domain stabilized conforming integration for thin beam and plate structures. Comput Mech 2011;48:47-63.

[48] Yoshida K, Sadamoto S, Setoyama Y, Tanaka S, Bui TQ, Murakami C, Yanagihara D. Meshfree flat-shell formulation for evaluating linear buckling loads and mode shapes of structural plates. J Mar Sci Tech 2017;22:501-12.

[49] Sadamoto S, Tanaka S, Taniguchi K, Ozdemir M, Bui TQ, Murakami C, Yanagihara D. Buckling analysis of stiffened plate structures by an improved meshfree flat shell formulation. Thin-Walled Struct 2017;117:303-13.

[50] Ozdemir M, Sadamoto S, Tanaka S, Okazawa S, Yu TT, Bui TQ. Application of 6-DOF meshfree modeling to the linear buckling analysis of stiffened plates with curvilinear surface. Acta Mech 2018;229:4995-5012.

[51] Sadamoto S, Ozdemir M, Tanaka S, Taniguchi K, Yu TT, Bui TQ. An effective meshfree reproducing kernel method for buckling analysis of cylindrical shells with and without cutouts. Comput Mech 2017;59:919-32.

[52] Ozdemir M, Tanaka S, Sadamoto S, Yu TT, Bui TQ. Numerical buckling analysis for flat and cylindrical shells including through crack employing effective reproducing kernel meshfree modeling. Eng Anal Bound Elem 2018;97:55-66.

[53] Tanaka S, Suzuki H, Sadamoto S, Imachi M, Bui TQ. Analysis of cracked shear deformable plates by an effective meshfree plate formulation. Eng Fract Mech 2015;144:142-57.

[54] Tanaka S, Suzuki H, Sadamoto S, Sannomaru S, Yu TT, Bui TQ. J-integral evaluation for 2D mixed-mode crack problems employing a meshfree stabilized conforming nodal integration method. Comput Mech 2016;58:185-98.

[55] Tanaka S, Suzuki H, Sadamoto S, Okazawa S, Yu TT, Bui TQ. Accurate evaluation of mixed-mode intensity factors of cracked shear-deformable plates by an enriched meshfree Galerkin formulation. Arch Appl Mech 2017;87:279-98.

[56] Tanaka S, Dai MJ, Sadamoto S, Yu TT, Bui TQ. Stress resultant intensity factors evaluation of cracked folded structures employing 6DOF meshfree modeling. Thin-Walled Struct 2019;144:106285.

[57] Sadamoto S, Ozdemir M, Tanaka S, Bui TQ, Okazawa S. Finite rotation meshfree formulation for geometrically nonlinear analysis of flat, curved and folded shells. Int J Non-linear Mech 2020;119:103300.

[58] Noguchi H, Kawashima T, Miyamura T. Element free analyses of shell and spatial structures. Int J Numer Meth Eng 2000;47:1215-40.

[59] Organ D, Fleming M, Terry T, Belytschko T. Continuous meshless approximations for nonconvex bodies by diffraction and transparency. Comput Mech 1996;18:225-35.

[60] Joyot P, Trunzler J, Chinesta F. Enriched reproducing kernel approximation: Reproducing functions with discontinuous derivatives. Lecture Notes in Comput Sci and Eng 2005;43:93-107.

[61] Ishikawa H. A finite element analysis of stress intensity factors for combined tensile and shear loading by only a virtual crack extension. Int J Fract 1980;16:R243-46.

[62] Raju IS, Shivakumar KN. An equivalent domain integral method in the two-dimensional analysis of mixed mode crack problems. Eng Fract Mech 1990;37:707-25.

[63] Dirgantara T, Aliabadi MH. Stress intensity factors for cracks in thin plates. Eng Fract Mech 2002;69:1465-86.

[64] Dirgantara T. Boundary element analysis of crack in shear deformable plates and shells. PhD thesis, University of London; 2000.

[65] Rice JR. A path independent integral and approximate analysis of strain concentration by notches and cracks. J Appl Mech 1968;35:379-86.

[66] Chen JS, Wang D. A constrained reproducing kernel particle formulation for shear deformable shell in Cartesian coordinates. Int J Numer Meth Eng 2006;68:151-72.

[67] Wang D, Song C, Peng H. A circumferentially enhanced Hermite reproducing kernel meshfree method for buckling analysis of Kirchhoff-Love cylindrical shells. Int J Struct Stabil Dynam 2015;15:1450090.

[68] Hibbitt, Karlsson, Sorensen, Inc. ABAQUS/standard user's manual, v. 6.5. Pawtucket, Rhode Island; 2004.

[69] Folias ES. On the effect of initial curvature on cracked flat sheets. Int J Fract Mech 1969;5:327-46.

[70] BS 7910. Guide to methods for assessing the acceptability of flaws in metallic structures. British Standards Institution; 2005.